Geochemistry, Geophysics, Geosystems®

RESEARCH ARTICLE
10.1029/2024GC011519

Assessing the Helium Potential of Variscan Batholiths: Insight From Corsica Island

H. Dutoit[1], F. V. Donzé[1], C. Cardoso[2], J. Charroy[1], C. Riba Pereyra[1], A. Taillefer[1], C. Dusséaux[3], D. Tisserand[1], L. Monnier[4], S. Byrdina[1], R. Pik[2], and L. Truche[1]

[1]ISTerre, USMB, UGE, CNRS, IRD, Université Grenoble Alpes, Grenoble, France, [2]CNRS, CRPG, Université de Lorraine, Nancy, France, [3]Chrono-Environnement UMR6249, CNRS, Université de Franche-Comté, Besançon, France, [4]GET, CNRS, IRD, UPS, CNES, Toulouse University, Toulouse, France

Abstract Most of the current helium (He) reserves originate from fortuitous discoveries, mainly made during oil and gas exploration in sedimentary basins. As helium generation depends on U and Th α-decay, old geological provinces gather key ingredients for high He accumulation. However, numerous He-rich springs have also been documented in much younger rocks, such as Variscan granites (320–250 Ma). These latter discoveries question the current exploration guidelines and require revisiting some of the longstanding paradigms. Here, is investigated He migration along a major fault rooted in the Corso-Sardinian batholith (France). Two thermal springs, Caldanelle and Guagno-Les-Bains, show significant outgassing activities of crustal sourced He with concentrations up to 1.45 vol% and flow rates of 110 m^3 STP ^{4}He/year. Besides He, the gas phase is dominated by N_2 (≈98 vol%) and minor CH_4. Based on a survey employing multidisciplinary methodologies, it is revealed that (a) Variscan rocks represent efficient ^{4}He source rocks, (b) the main source of He comes from the underlying Eo-Variscan basement, (c) A deeply rooted fault and dense fractures networks drain the He, (d) the helium loss is limited, (e) faults and fractures may act as partial traps, and finally (f) the presence of an efficient trap could promote a He-rich reservoir with high flux but low reserves. In that sense, young post-orogenic granites represent promising helium plays. The geological context in which Caldanelle and Guagno-Les-Bains are embedded is ubiquitous in European Variscan batholiths. This case study is therefore intended to serve as a guide for helium exploration and to provide insights into helium behavior within a Variscan geological context.

Plain Language Summary Helium, a crucial commodity for various industries, is mainly discovered by chance during oil and gas explorations. However, some thermal springs show high helium concentrations in young Variscan granites, opening new perspectives for helium exploration. This study examined helium migration along a major fault in the Corso-Sardinian batholith. Two thermal springs, Caldanelle and Guagno-Les-Bains, emit substantial crust-derived helium, reaching concentrations up to 1.45% by volume and a flow rate of 110 cubic meters per year of helium. These springs also contain mostly nitrogen (about 98%) and minor methane. The results show that Variscan rocks are potential plays for helium exploration. The primary helium source lies beneath these rocks. A deep fault zone associated with dense fracture networks facilitates helium drainage with minimal loss. Moreover, faults and fractures might also partially retain helium and contribute to its accumulation. The geological context observed in Caldanelle and Guagno-Les-Bains is widespread in European Variscan batholiths; thus, understanding helium behavior in these settings could guide future exploration strategies.

Key Points:

- Combined geological, geophysical and geochemical analysis of two Corsican He-rich thermal springs
- Deep faults and dense fracture networks allow for efficient fluid migration with limited loss
- Variscan geological context could be promising helium plays

Supporting Information:

Supporting Information may be found in the online version of this article.

Correspondence to:

H. Dutoit,
hugo.dutoit@univ-grenoble-alpes.fr

Citation:

Dutoit, H., Donzé, F. V., Cardoso, C., Charroy, J., Riba Pereyra, C., Taillefer, A., et al. (2024). Assessing the helium potential of Variscan batholiths: Insight from Corsica Island. *Geochemistry, Geophysics, Geosystems*, *25*, e2024GC011519. https://doi.org/10.1029/2024GC011519

Received 22 FEB 2024
Accepted 25 JUN 2024

Author Contributions:

Conceptualization: H. Dutoit, L. Truche
Data curation: H. Dutoit, F. V. Donzé, C. Cardoso, J. Charroy, C. Riba Pereyra, A. Taillefer, D. Tisserand, L. Monnier, S. Byrdina, R. Pik
Formal analysis: H. Dutoit, F. V. Donzé, C. Cardoso, J. Charroy, C. Riba Pereyra, A. Taillefer, D. Tisserand, S. Byrdina, R. Pik
Funding acquisition: F. V. Donzé, L. Truche
Investigation: H. Dutoit, F. V. Donzé, C. Cardoso, J. Charroy, C. Riba Pereyra, A. Taillefer, C. Dusséaux, L. Monnier, L. Truche

1. Introduction

Helium (He) exhibits a set of distinctive physicochemical properties that render it indispensable for a range of specialized applications including cryogenics, medical imaging, and advanced scientific research. This noble gas is primarily retrieved as a secondary product during the extraction of natural gas, thereby limiting exploration efforts to geological contexts relevant to hydrocarbon resources (Danabalan et al., 2022). Helium is now targeted by junior companies as a primary product in geological contexts that are not necessarily associated with hydrocarbon resources. This is the case in the Morvan Variscan batholith, France (45-8 Energy), in the East Africa rift system in Tanzania (Helium one), and the Mid-Continent Rift in Minnesota, USA (Pulsar Helium Inc). Sedimentary basins draping Precambrian granitic basements are also promising for exploration, as is the case in

Methodology: H. Dutoit, F. V. Donzé, C. Cardoso, J. Charroy, A. Taillefer, D. Tisserand, S. Byrdina, R. Pik, L. Truche
Supervision: H. Dutoit, F. V. Donzé, L. Truche
Validation: H. Dutoit, F. V. Donzé, L. Truche
Visualization: H. Dutoit
Writing – original draft: H. Dutoit

Saskatchewan (Canada) (Yurkowski, 2016). However, despite these new plays for He exploration, the world production of this element still relies on hydrocarbon production.

Consequently, the majority of helium reservoirs that have been systematically investigated and modeled are situated within intra-cratonic sedimentary basins, frequently targeted for hydrocarbon exploration (Brown, 2019; Cheng et al., 2023; Dong et al., 2019). Within these geological settings, helium concentrations seldom surpass 1 vol%, yet the large volumes of co-extracted natural gas make its extraction economically viable (Figure 1). However, global demand for helium has been experiencing a consistent upward trajectory, while production is struggling to keep pace (Cai et al., 2010; Olafsdottir & Sverdrup, 2020; Provornaya et al., 2022). Given the growing imbalance between supply and demand, there is an emergent need to diversify helium sourcing by investigating alternative geological environments, thereby mitigating the industry's reliance on hydrocarbon extraction.

The helium system can be conceptualized within the classical triad that delineates the formation of most georesources: source, migration, and trap. Helium is primarily generated through the radioactive decay of uranium and thorium isotopes (Ballentine & Burnard, 2002). Consequently, rocks of Precambrian to Archean age are often identified as the most fertile source rocks due to their elevated radioelement concentrations and extended geological residence times, which facilitate helium accumulation. Intriguingly, helium-rich geological fluids have also been discovered in considerably younger Variscan-age formations. Notably, helium gas concentrations exceeding 1 vol% have been documented in springs and geothermal wells situated within batholithic settings (Batard et al., 1982; Hao et al., 2023; Risler & Batard, 1978). The underlying mechanisms for these anomalous concentrations remain poorly understood, although it is hypothesized that a complex interplay exists between the source rocks' efficiency, the migration pathways, the helium loss, and eventual accumulation sites. Therefore, beyond the source rock itself, multiple auxiliary factors significantly influence helium resource formation. These include thermal history, local and global tectonic regimes, drainage properties, and the presence of trapping formations. Despite compelling geological evidence, comprehensive characterization and modeling of these helium systems remain conspicuously limited.

In addition, helium and noble gases in general serve as critical geochemical proxies for understanding crust-mantle interactions involving thermal waters. Specifically, helium isotopic ratios act as tracers for deep-seated sources and fault systems, thus offering valuable insights into the mechanisms of deep gas emissions (Ballentine & Burnard, 2002). Often correlated with thermal anomalies, these emissions provide indicators of the spatial distribution and geochemical characteristics of subsurface reservoirs and heat sources. Owing to a unique confluence of geological features—such as an extensive continental crust, Variscan magmatic intrusions, and associated networks of crustal and lithospheric fractures—Corsica presents an advantageous setting for the comprehensive study of the interplays among heat sources, tectonic activity, and deep-fluid dynamics.

This investigation focuses on two thermal springs situated in the western Variscan region of Corsica: Caldanelle and Guagno-Les-Bains (hereafter Guagno). Situated to the north of Ajaccio and in close proximity to Vico, these springs exhibit pronounced helium degassing despite the geologically recent nature of the surrounding formations. Both sites present optimal conditions for sampling, facilitated by existing infrastructure such as boreholes and bubbling pools, as well as their intrinsic characteristics of undisturbed artesian flows. These attributes make Caldanelle and Guagno exceptional sites for the comprehensive analysis of geothermal fluid migration and associated He dynamics.

This study is based on an integrative multidisciplinary methodology with the objective of delineating and modeling the sources and migration pathways of thermal water and associated gases. Concurrently, the research aims to develop efficacious methodologies for helium exploration within these particular geological settings while quantitatively evaluating their helium resource potential.

2. Geological Setting

Spanning the late Carboniferous to early Permian periods, the collisional phase of the Variscan orogeny brought the tectonic juxtaposition of the Panafrican and Eo-Variscan basement rocks (Figure 2). This tectonic event was succeeded by a phase of intense magmatic activity, culminating in the formation of multiple batholiths, including the Corso-Sarde batholith (e.g., Rossi et al., 2015). Both the Panafrican and Eo-Variscan basements underwent varying degrees of metamorphism. The Panafrican basement is chiefly composed of micaschists and

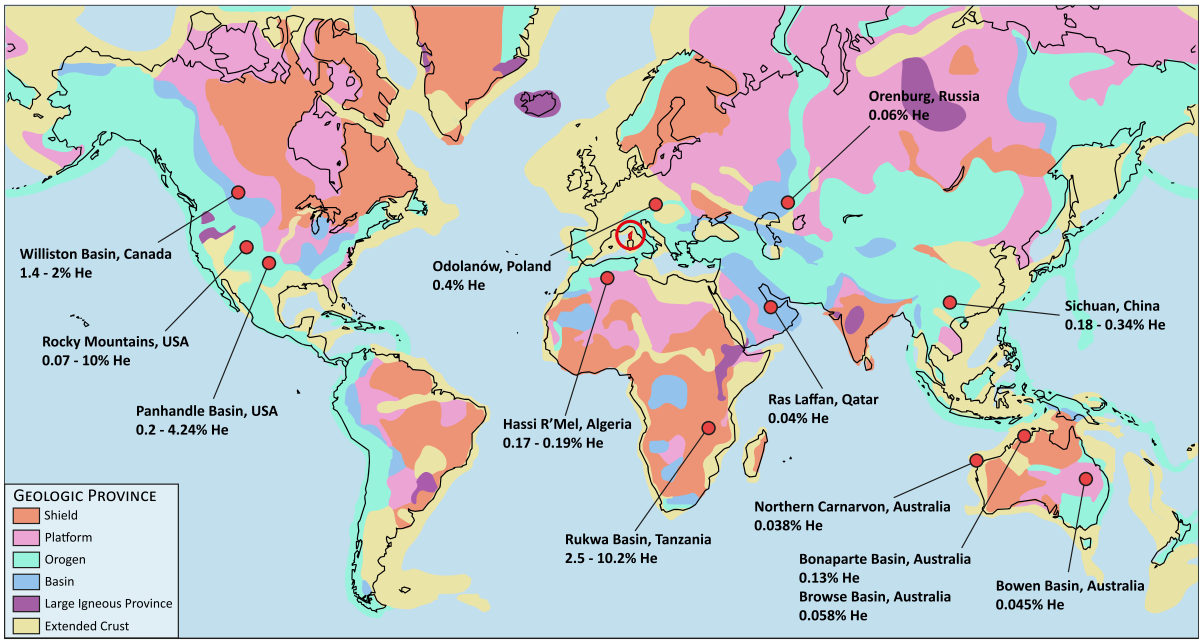

Figure 1. Major helium (He) production sites and average (or range) He concentrations in their geological settings. Corsica Island is circled in red. Geological map courtesy of the US Geological Survey.

amphibolites, which are unconformably overlain by Ordovician conglomerates and Silurian schists. In contrast, the Eo-Variscan basement consists of ortho- and para-derived gneisses interspersed with eclogitic relics.

Three distinct magmatic bodies (U1, U2, and U3) were emplaced at varying depths during a large-scale uplift event following the nomenclature of Rossi et al. (2015). The initial magmatic cycle, characterized by Mg-K U1 granitoids (350–330 Ma), occurred at the fragile-ductile interface, where the lower crust experienced partial melting due to adiabatic ascent. This phase of magmatism induced anatexis in the Eo-Variscan basement. Unlike the U1 unit, the genesis of the calc-alkaline U2 granitoids (310–280 Ma) is associated with post-thickening crustal extension (Cortesogno et al., 1998; Rossi & Cocherie, 1991). The magmatic activity concluded during the Lower Permian (288–280 Ma) with the emplacement of U3 alkaline magmatism within a thinning crust. Concurrent with these magmatic phases were several basic intrusions, which are observed in association with the Mg-K U1 granitoids, the calc-alkaline U2 granitoids and the alkaline U3 granitoids along a NE-SW trend (Caritg et al., 2009).

In the vicinity of Vico, the Eo-Variscan Mercolaccia gneiss is exposed flanked by U1 and U2 granitoids. Within this region, the granitoids occur as biotite- and/or amphibole-rich monzonites, leucomonzogranites, and granodiorites. These are accompanied by basaltic intrusions as well as veins of microgranite and quartz (Rossi et al., 2010). Caldanelle and Guagno are both located at the junctions of three distinct granitic lithologies, intersected by a series of E-W faults and N-S to NE-SW relay structures (Figure 3). These late strike-slip fault orientations, which predate Permian volcanism, are ubiquitously observed across multiple scales in the majority of Variscan batholiths (Figure 3). Originating from N-S to NW-SE compressional forces, these faults can reach amplitudes covering several kilometers and may extend deep into the pre-batholithic basement. Subsequent tectonic episodes reactivated these faults: first as normal faults during Mesozoic sedimentation, and later as reverse faults during Alpine orogenic compression. These fault systems also exerted a significant influence on the emplacement and structural organization of the various granitoid bodies (Arthaud & Matte, 1975).

3. Materials and Methods

3.1. Field Conditions

Caldanelle and Guagno springs were sampled for both water and gas, and their respective flow rates were quantified. Caldanelle is an artesian spring located in a small tiled basin featuring a crack at the bottom through

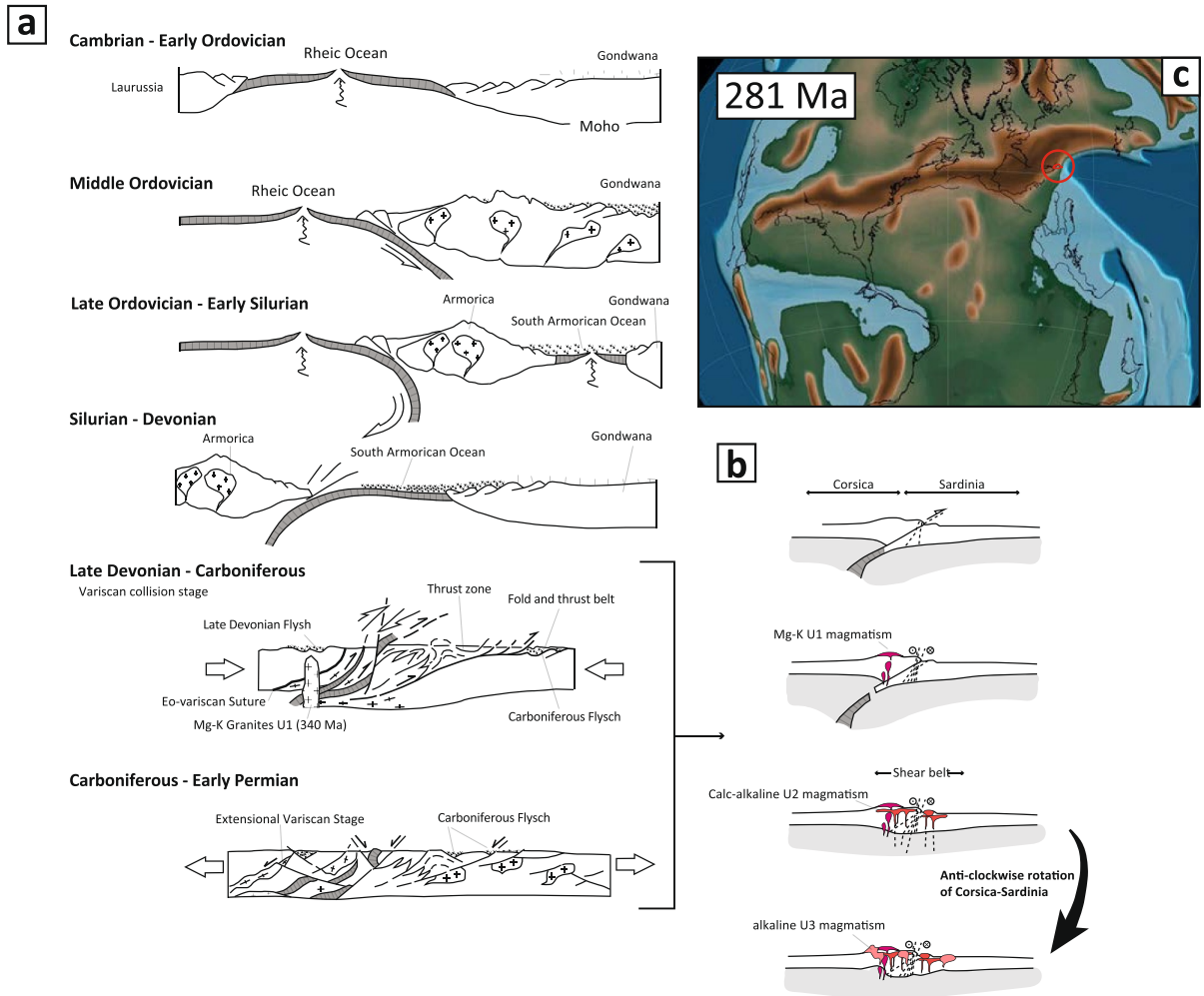

Figure 2. (a) Schematic diagrams of the geodynamic evolution of the Corso-Sardinian block during the Paleozoic (Rossi et al., 2010). (b) Geodynamic evolution of the Corsica-Sardinia block in Variscan times (Casini et al., 2015). (c) Panafrican and Eo-Variscan contact reconstruction where Corsica is located on the equator line and circled in red (Scotese & van der Pluijm, 2020).

which gas bubbles escape. Guagno features both a 120-m deep borehole and an artesian spring known as Venturini. Caldanelle, being remote and distant from potential anthropogenic noise sources, was selected for geophysical investigations.

3.2. Water and Gas Sampling and Analytical Procedures

Dissolved ions. Water samples from each site were collected, filtered through 0.2 µm hydrophilic PTFE filters and stored in polyethylene bottles for subsequent chemical analyses. To stabilize the samples for cation and anion measurements, they were treated with either Suprapur® 65 vol% HNO_3 (0.15 ml per 50 mL of water) or zinc acetate (0.5 ml at a concentration of 0.01 mol/L per 50 ml of water), respectively. These samples were stored at 4°C in dark conditions and analyzed a month after sampling. Additional samples stabilized with zinc acetate were taken for the assessment of alkalinity and dissolved sulfides. Field blanks were prepared on site using ultra-pure water (resistivity 18.2 MΩ cm) and following identical protocols. On-site measurements for temperature, pH, and redox potential (Eh) were conducted using multi-parametric probes (WTW MultiLine P4 equiped with a SenTix® ORP redox Ag/AgCl probe) that were calibrated onsite with appropriate standard solutions.

Analytical procedures for cations (including Ca, K, Mg, Na, Si, Sr, Al, As, Au, B, Ba, Cd, Co, Cr, Cu, Fe, Hg, Li, Mn, Mo, Ni, P, Pb, Sb, Se, Te, and Zn) were performed using an ICP-AES Varian 720-ES (Agilent®). Anion concentrations (F^-, Cl^-, NO_3^-, SO_4^{2-}, NO_2^-, Br^-, and PO_4^{3-}) were quantified using a Dionex Integrion HPIC®

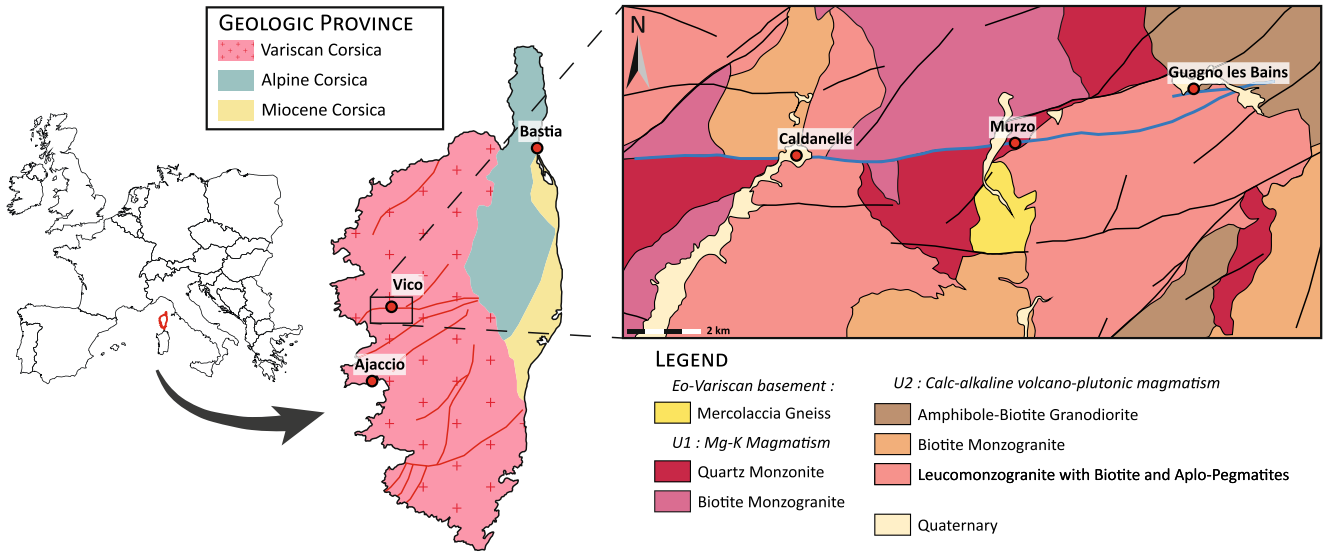

Figure 3. Simplified geological map of Corsica and the Vico region showing the location of Caldanelle and Guagno-les-Bains springs. The Vico fault is highlighted in blue.

ion chromatograph. Total dissolved sulfide concentration (ΣH_2S) which mainly represents the sum of aqueous H_2S, HS^- and S^{2-}, was determined through the methylene blue method (Cline, 1969). The resultant blue complex was detected using a double-beam UV-Vis spectrophotometer Cary 3500 Multicell from Agilent®. Alkalinity was quantified via Gran titration using HCl (at 0.1 mol/L). Instrument calibrations were performed prior to analyses, employing multiple certified standards at varying dilution levels commensurate with the concentration ranges of the elements under investigation. For trace elements, the lowest measurable concentrations were targeted with the lowest calibration point reachable by the machine, that is, at 0.01 mg/L for Al, B, Cd, Co, Cr, Cu, Fe, Mn, Mo, Ni, Pb, Sb, Zn, at 0.03 mg/L for As, Ba, Hg, Li, P, Se, Te and at 0.05 mg/L for Au. Accuracy was determined with double calibration and precision with repeated analysis of the same standard to target results with 5% uncertainty at the 95% confidence level and an ion balance lower than 5%.

Free and dissolved gases. In Caldanelle, gas bubbles emanating from the spring were captured in 10 mL glass vials using the water displacement technique. These vials were sealed underwater with a thick rubber septum and aluminum collar to prevent air contamination (Figure 4a). In contrast, in Guagno, gas accumulates at the extrados of a curved horizontal stainless steel pipe, which is directly connected to the borehole's wellhead. A valve facilitates the direct sampling of gas into either gas bags (Cali-5-bond, Calibrated Instrument, Inc.®) or vacuum gas cylinders (40 mL stainless steel 316L Swagelok gas cylinders). The gas composition was analyzed using a Perkin Elmer® CLARUS 500 Gas Chromatograph (GC) equipped with a thermal conductivity detector calibrated for He, H_2, O_2, N_2, CO, CH_4, and CO_2. The GC is equipped with a 2-m-long column (RESTEK® Shin Carbon ST 80/100) through which argon served as the carrier gas. The analyses of $^4He/^{20}Ne$ and $^3He/^4He$ ratios of water and gas sampled in copper tubes were performed, respectively, on a MKS Microvision 2 quadrupole mass spectrometer (QMS) and a split flight tube noble gas mass spectrometer (Helix SFT - Thermo Fisher Scientific) at the Centre de Recherches Pétrographiques et Géochimiques (CRPG) noble gas analytical facility (Mabry et al., 2013). The standard deviation of the $^3He/^4He$ ratios was 2.26% based on the replicate analysis of standard He (atmospheric). Results are corrected for blanks, which contributed <0.1% of the total He abundances.

For dissolved gas measurements, water was collected in 120 mL glass vials, which were sealed underwater using a thick rubber septum to ensure an air-free sample. In the laboratory, a determined volume of water was replaced with pure argon and the sample was agitated for 1 hour to allow the exsolution of dissolved gases into the headspace. The composition of the resulting headspace was analyzed using the Perkin Elmer® CLARUS 500 GC. Using the known headspace composition and Henry's law constants for the involved species (at 25°C and 1 atm), the quantity of dissolved gas in the remaining water volume was calculated. For comparative purposes, in situ measurements of dissolved gases in Guagno were performed using a QMS MiniRuedi (Gasometrix®) equipped with a GE-MIMS degassing module (Figure 4b).

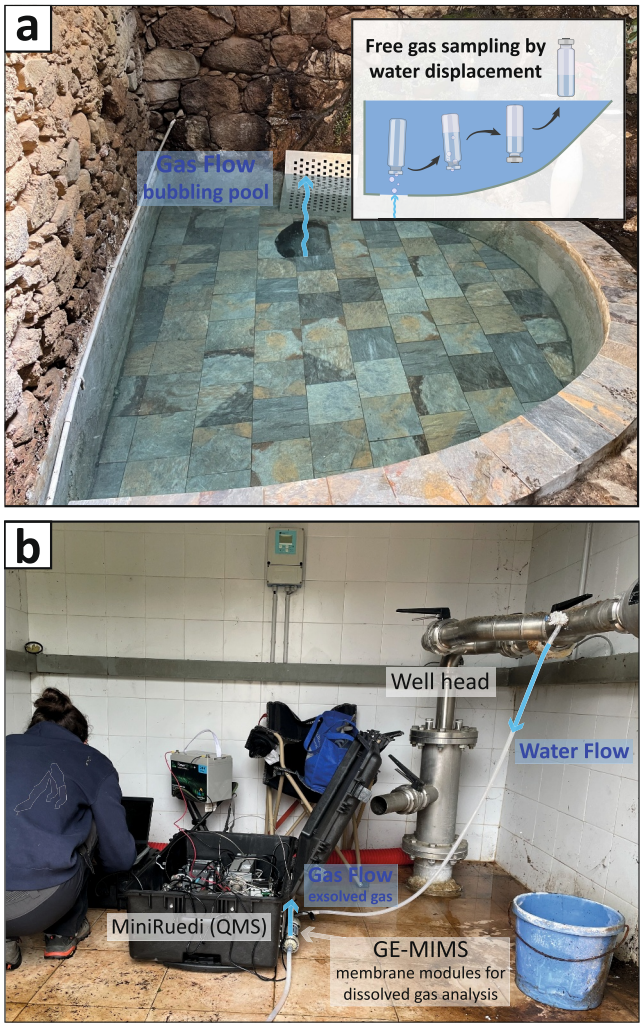

Figure 4. (a) Caldanelle bubbling pool. (b) Guagno-Les-Bains borehole during dissolved gas analysis.

Gas flow rates in both Guagno and Caldanelle were determined by replacing a known volume of water measured using a graduated bottle and funnel over a specified time interval (water displacement method). In Caldanelle, water flow rates were calculated based on the spring's discharge rate. For Guagno, water flow rate data were obtained from historical in situ measurements for both the borehole and Venturini spring, which have remained stable over several years.

Bulk rock composition. In an attempt to identify the source of helium, the four granitoids that outcrop around the two springs were collected for analysis of uranium ([U]), thorium ([Th]), and lithium ([Li]) concentrations. Only the least-altered cores of hand specimens, ranging from 10 to 20 cm in diameter, were selected for crushing and subsequent analysis. These measurements were conducted at the SARM facility at the CRPG in Nancy (France) utilizing an ICP-MS iCapQ for analytical quantification.

3.3. Geophysical Methods: EMI and MT

Frequency domain electromagnetic induction method (EMI) uses alternating magnetic fields, which are generated and recorded by two induction coils, to study the resistivity structure of the shallow subsurface of the Earth (typically, tens of meters). The primary magnetic field operated by the transmitter induces electrical eddy currents in the Earth, which in turn generate secondary magnetic field recorded by the receiver. The relationship between the primary and secondary fields gives information on the electric resistivity of the subsurface. The depth of investigation depends on the transmitted frequency and distance between the transmitter-receiver coils (e.g., Nabighian, 1988; Sumner, 2012). The response of these induced fields is contingent on the electrical conductivity and magnetic permeability of the subsurface materials, thereby serving as the foundational principles for subsurface imaging. Various geological factors, including but not limited to mineralogical composition, soil moisture content, and the extent of fracturing, exert influence on these geophysical parameters (Doolittle & Brevik, 2014).

The electromagnetic (EMI) survey was carried out using the CMD-DUO, an electromagnetic conductivity meter developed by GF Instruments® (GF Instruments®, 2020). This dual-operator probe offers selectable depth ranges, enabling variable exploration depths of either 15/7.5 m, 30/15 m, or 60/30 m. Operating at a single frequency of 925 Hz, the instrument uses fundamental electromagnetic induction techniques to acquire high-resolution measurements of apparent conductivity and magnetic susceptibility.

Three EMI profiles, ranging from 100 to 200 m long, were carried out in the field located right above the main emergence of Caldanelle spring (Figure 5b). Each profile was subdivided into 5-m sections, which defined the measurement points. To enhance depth sensitivity, measurements within each transect were conducted in three sequential steps, featuring transmitter-receiver distances of 10 m, 20 m, and 40 m. Guided by the structural data from the 1/50,000-scale geological map provided by BRGM and field observations, two profiles were oriented along the N-S axis, while the third was aligned at N135 to perpendicularly intersect structures at N90 and N45.

The inversion of EMI ground survey data was performed using the EMagPy software (McLachlan et al., 2021), which employs a mathematical approach to construct a subsurface model based on the collected CMD-DUO data (GF Instruments®, 2016). This inversion process aims to resolve Maxwell's equations iteratively to minimize discrepancies between observed and computed data. The software's nonlinear inversion algorithm enhances model robustness by accommodating a range of geophysical conditions. Additionally, regularization techniques are employed to mitigate underestimation of the ill-posed inverse problem, trying to ensure physically plausible solutions by smoothing. A key advantage of this software is its efficient inversion algorithm capable of handling complex 2D and 3D data sets, thereby facilitating a comprehensive and accurate characterization of the subsurface based on EM survey data.

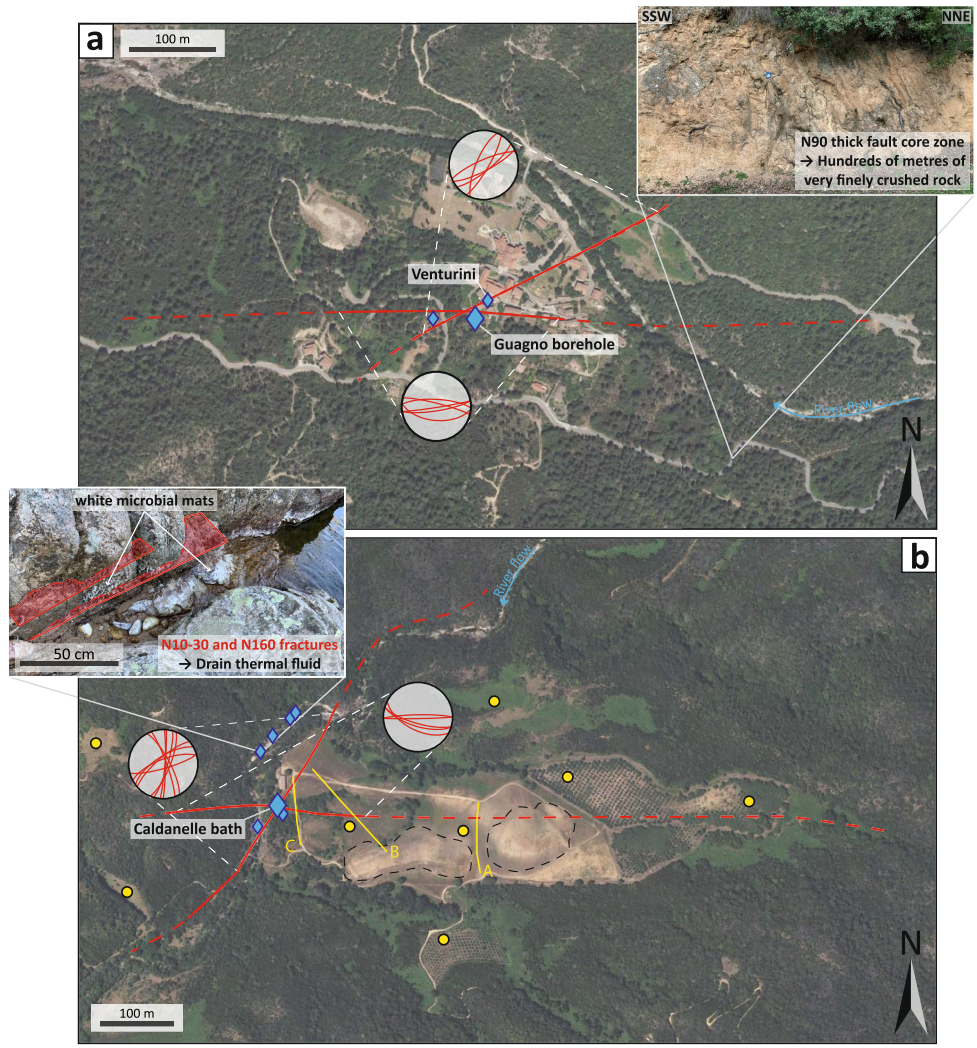

Figure 5. (a) Satellite view of Guagno-Les-Bains. The big blue diamond corresponds to the borehole, and the two small diamonds correspond to the historic artesian springs (the one to the west being presently dry). The faults are in red and the planes plotted in the canvas are a compilation of the planes measured in the field, sorted by orientation. (b) Satellite view of the Caldanelle area showing the location of the main (blue diamond) and secondary (small blue diamonds) springs. The dotted black lines delimit arenized granite domes. The faults are in red and the planes plotted in the canvas are a compilation of the planes measured in the field, sorted by orientation. The yellow lines correspond to the EMI cross-sections A, B and C, and the yellow dots are the MT measurement points.

The Magnetotelluric (MT) method is a passive electromagnetic geophysical technique originally developed by Tikhnov (1950) and further refined by Cagniard (1953). This method involves simultaneous measurements of the natural variations of the Earth's magnetic field and the electric field induced in the Earth by these variations (e.g., Chave & Jones, 2012). The target parameter of the MT method is a four-component tensor of electromagnetic impedance, intimately related to the electrical resistivity. The impedance tensor is frequency dependent and is formed by ratios between horizontal components of electric field and horizontal components of magnetic field. A fundamental assumption underlying this technique is that incident electromagnetic waves can be approximated as plane waves, which allows us to establish a straightforward relationship between the frequency and the depth. The depth of investigation depends on the conductivity of the rocks and the frequency of observation, with the high frequency variations decaying more rapidly due to the so-called skin effect. The MT method is especially sensitive to electrically conductive bodies imbedded in a resistive matrix, while it is nearly blind to resistive structures imbedded in a conductive matrix. This particularity of the MT method makes it especially interesting to detect electric conductors such as deep fluids or mineral alteration zones.

Magnetotelluric (MT) data were collected (end of March-beginning of April 2023) at eight distinct locations in close proximity to the Caldanelle hot spring (Figure 5b) using two instruments from Phoenix Geophysics® with broadband induction coils MTC-155 and MTC-185, as well as 24-bit MTU-5C data loggers. The survey encompasses a spatial extent of 1.2 km in the east-west direction and 400 m in the north-south direction. Data were acquired in a frequency range spanning approximately 10 kHz to 0.001 Hz, utilizing broadband measurements with a maximum acquisition rate of 24 kHz.

All data were recorded overnight. Subsequent bi-variate robust single-site processing was performed using Phoenix EMPower2® software. The recording protocol included continuous measurements at a rate of 150 samples per second interspersed with 2-s intervals at 24,000 samples per second every 30 s. Then, the software quality criteria facilitate the exclusion of noise-induced data clusters both in time and in frequency domain. Namely, in frequency domain, the data with low coherency between the magnetic and electric fields were eliminated as well as the data with an unphysical phase between the magnetic and electric fields. In the time domain, the spikes and events with extremely high amplitudes were eliminated. The obtained transfer functions were still contaminated by obvious outliers. Therefore, (a) one site was rejected, (b) the frequencies below 2 s were disregarded, and (c) only off-diagonal elements of the impedance with high values of the errors (15%) were used for 3D inversion, neglecting the noisier main-diagonal elements and tippers.

One-dimensional (1D) stochastic inversions of the data at all sites were first performed using the RJMCMCMT reversible jump Monte-Carlo Markov Chain code (Brodie & Jiang, 2018). The stochastic inversion has the advantage of being able to explore the whole space of parameters (depths and an invariant of the impedance), while this is impossible in 3D inversion, bound to stay close to a preliminary chosen prior model. In addition, the preliminary 1D model allows to identify the adequate value of the prior model for the 3D inversion.

The 3D inversion was performed with the ModEM code (Kelbert et al., 2014), and topography was considered constructed based on the BDAlti model with 25 m spatial resolution. The 3D grid was constructed with dimensions of $49 \times 53 \times 50$ cells in the X, Y, and Z directions, respectively. The X-axis was aligned with UTM east, and the Y-axis with UTM north, the minimal cell size in the z-direction was 30 m, to allow an accurate consideration of the topography. The inversion scheme included the following steps:

1. Inversion of the phase tensor only (a part of the impedance tensor not sensitive to near-surface galvanic distortion) using a non-linear conjugate gradient (NLCG) algorithm with a "roughness" control parameter α of 0.4 and a prior model with a uniform resistivity of 1 kΩ m.
2. Forward-modeled impedances were then produced and compared against the full impedance data to control and edit static shift manually.
3. The edited full impedance tensor was then inverted with a "roughness" control parameter α of 0.4, using the output of the first step as the prior model.
4. The roughness control parameter α was then reduced to 0.2 before running a new series of NLCG inversions using the output of step 3 as the prior model. The resulting model had an RMS of 2.4.

4. Results

4.1. Field Observations

As illustrated in Figure 2, the Caldanelle and Guagno springs are located along a major E-W fault spanning approximately 30 km. At Murzo, situated equidistantly between the two hot springs, an outcrop reveals the core zone of this extensive fault, manifesting as a 20-m-thick layer of fine-grained clay fault gouge. Within this core zone, the majority of fault planes exhibit sub-vertical orientations, ranging from N70 to N130, with minor occurrences at N30 and N150 to N160 (Figure S1 in Supporting Information S1). This core zone is also observable at the entrance to Guagno and 2 km east of the village along the road (Figure 5a). Here, fault planes oriented at N160 are more prevalent, and the core zone appears to be 10 times thicker than that in Murzo. Fracture orientations are more heterogeneous, varying from N20 to N160, but tend to align along two principal directions: N90 and N30 (Figure 5a). These observations are consistent along the entire length of the mapped E-W fault, with the exception of Caldanelle where only a few E-W-trending fracture planes were identified, whereas N30 orientations dominate in both faults and fracture planes (Figure 5b).

In Caldanelle, where rock exposures are well-preserved due to river erosion, minor water seepages are observable along the river bed along certain fractures (Figure 5b). These are accompanied by the presence of white microbial

Table 1
Chemical Compositions in mg/L and Physical Parameters of Caldanelle and Guagno (Borehole and Venturini) Waters

Samples	pH	Temp °C	EC µS cm^{-1}	Eh mV	Ca^{2+} mg L^{-1}	K^{+}	Na^{+}	Li^{+}	Sr^{2+}	Al^{3+}	Si	B	Mo	F^{-}	Cl^{-}	SO_4^{2-}	HCO_3^{-}	CO_3^{2-}	H_2S
Caldanelle	8.87	32	591	−123	4.7	5.8	117	0.10	0.14	0.01	49.7	0.07	0.02	12.7	45.8	109	67.1	9	3.48
Guagno (B-120-m deep)	8.53	62	397	−78	3.9	3.4	78	0.04	0.05	0.01	44.3	0.02	0.03	7.7	24.4	69	63.44	12	1.5
Venturini	8.86	57	435	61															

Note. NO_3^{-}, Br^{-}, and PO_4^{3-} as well as Au, Ba, Cd, Co, Cr, Cu, Hg, Mn, Pb, Sb, Se, Te, Zn were not detected. Mg, As, Fe, Ni, P were not quantifiable but present. The combined charge balance of the anions and cations add up to 0% and −1% for Caldanelle and Guagno respectively. EC stands for the conductivity and Eh for the redox potential (corrected relative to the potential of the standard hydrogen electrode (SHE): +207 mV at 25°C).

mats similar to those observed in Caldanelle's thermal baths as well as a faint odor of hydrogen sulfide (H_2S). These seepages predominantly emanate from fractures oriented at N10 to N30, and less frequently at N160, to the north of the main spring emergence. Fault planes with similar orientations have also been measured and appear to intersect the main spring.

4.2. Water and Rock Chemistry

The physicochemical characteristics of the waters from the investigated springs are reported in Table 1. Both Guagno and Caldanelle springs display similar ionic profiles; however, Caldanelle consistently demonstrates higher concentrations of cations and anions compared to Guagno with the exception of alkalinity. These springs predominantly exhibit a sodium-chloride geochemical signature typical of water-granitoids interaction (Figures 6a and 6b; Sonney, 2010) accompanied by noticeable concentrations of sulfate (SO_4^{2-}) and bicarbonate (HCO_3^{-}) ions, the latter's significant content probably preventing their classification as sulfate-rich waters according to Figure 6a. Caldanelle spring is characterized by a slightly higher pH value (8.87) and electrical conductivity (591 µS/cm), and lower redox potential (−123 mV) in comparison to Guagno's spring, which has a pH of 8.53, electrical conductivity of 397 µS/cm, and a redox potential of −78 mV. Notably, the emergence temperatures of the two springs differ substantially as Caldanelle and Guagno discharge water at 32 and 62°C, respectively.

The lithologies in the vicinity of these springs display characteristic concentrations of Uranium ([U]), Thorium ([Th]), and Lithium ([Li]) commonly associated with post-orogenic Variscan granites (Lucazeau, 1981; Lucazeau & Mailhé, 1986; Verdoya et al., 1998). Specifically, Uranium concentrations range from 2.77 to 10.2 ppm, while Thorium concentrations vary between 9.35 and 26 ppm (Table 2).

4.3. Gases Compositions and Flux

Caldanelle and Guagno springs have comparable free gas compositions, containing 1.4 vol% and 1.2 vol% of helium (He), respectively, with nitrogen (N_2) constituting over 98 vol% of the total volume of gas (Table 3). A notable distinction between the two springs lies in the concentration of methane (CH_4), which is an order of magnitude higher in Caldanelle compared to Guagno, albeit still at a low level. No long-term monitoring has been implemented to assess potential temporal fluctuations in these concentrations. Nevertheless, the data align well with previous measurements by Berthier et al. (1980). These gaseous species are also present in the dissolved phase within the water, with concentrations ranging from 51.5 to 52.5 µmol/kg$_w$ for He and 4,113–4,154 µmol/kg$_w$ for N_2. Given that the water flow rate substantially exceeds the gas flow rate, the majority of the annual He output is in the dissolved phase, accounting for approximately 98% of the total He discharge in both Caldanelle and Guagno. This observation is consistent for N_2 and CH_4 as well. For Guagno, the annual He-N_2-CH_4 production from the Venturini artesian spring was estimated using the same concentration parameters as those for the borehole nearby. Cumulatively, the annual He production (both dissolved and free) is estimated to be 492.91 mol/yr (11.08 m³ STP He/yr) for Caldanelle and 4393.17 mol/yr (98.78 m³ STP He/yr) for Guagno.

In Guagno, the $^3He/^4He$ isotopic ratios for free and dissolved helium are closely aligned, registering at 0.02 Ra and 0.03 Ra, respectively, where Ra denotes the atmospheric $^3He/^4He$ ratio of 1.4×10^{-6}. In contrast, Caldanelle exhibits a marginally elevated $^3He/^4He$ ratio of 0.06 Ra for its dissolved helium fraction. Notably, both springs

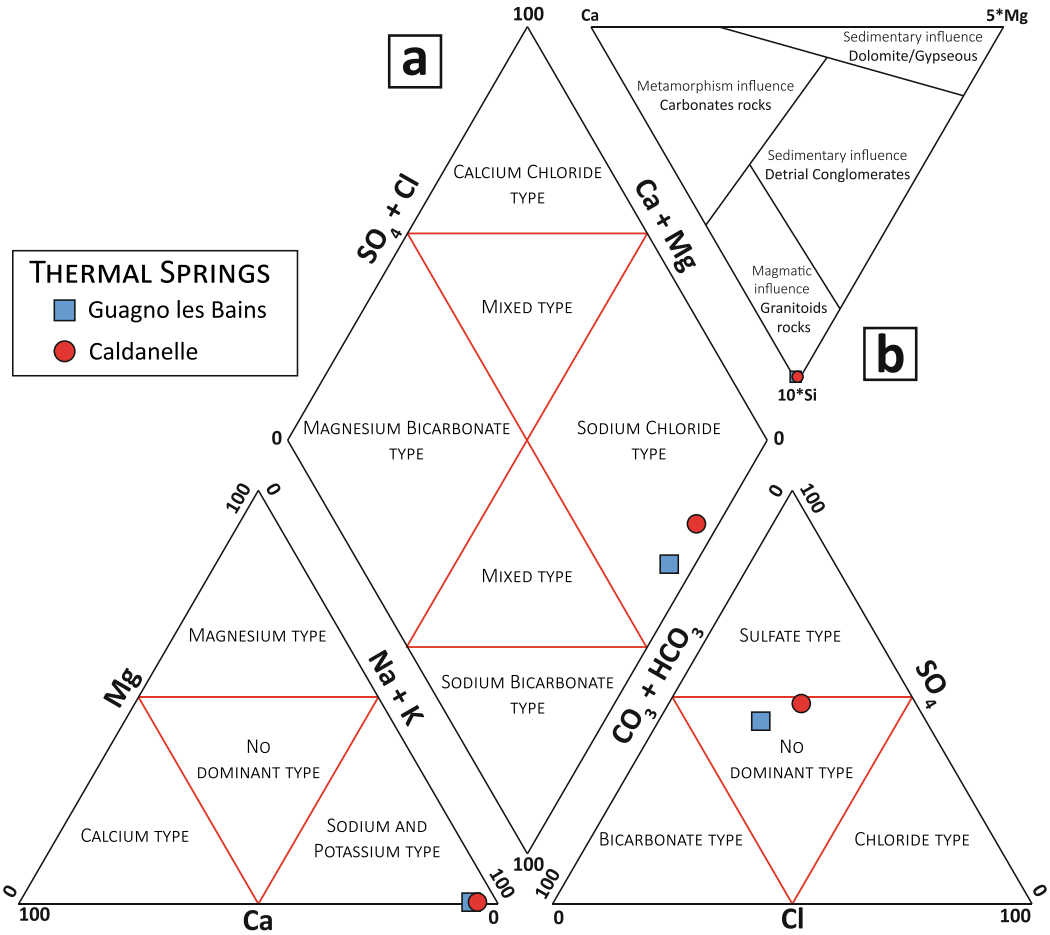

Figure 6. (a) Piper diagram, showing the main characteristic of the water chemistry of Caldanelle and Guagno springs. (b) Water-rock interaction ternary diagram (Derron & Pfeifer, 2018; Giggenbach, 1988) showing that the chemical profiles of the studied waters are consistent with circulation through a granitic basement.

manifest exceptionally high $^{4}He/^{20}Ne$ ratios, exceeding 30,000, which is substantially greater than the corresponding atmospheric ratio of 0.032 (Figure 8).

4.4. Geophysical Data

The acquired EMI cross-sections (Figure 9) reveal a range of electromagnetic resistivity values, extending up to 10,000 Ω m for the initial 60 m of depth. These sections can be divided into three distinct layers. The uppermost 10 m feature a thin highly resistive layer overlying a thicker highly conductive layer. Below this, a 40- to 50-m-thick layer exhibits heterogeneous resistivities ranging from 80 to 1,000 Ω m, punctuated by 10- to 30-m-thick rounded anomalies with resistivities of 10,000 Ω m. The final 5 m of the sections appear to indicate the upper boundary of a structure with resistivities similar to those of rounded anomalies. Figure S2 in Supporting Information S1 shows the raw EMI results and the misfit between the measurements and the resulting model.

The three-dimensional inversion model, derived from magnetotelluric (MT) data, provides a subsurface characterization down to a depth of 2 km. Despite minimal anthropogenic interferences in the surrounding area, the inversion results exhibit a degree of noise, thereby compromising depth resolution. However, the near-surface resolution—spanning from the elevation of the

Table 2
Li-U-Th Content of the Lithologies Surrounding Caldanelle and Guagno Springs (Samples Named After the 1:50,000 Geological Map of Vico-Cargèse From Rossi et al. (2010): Lγ3CA = Leucomonzogranite With Biotite, γ4CA = Amphibole-Biotite Granodiorite, γ3CA = Biotite Monzogranite, γMqL = Quartz Monzonite) With Their Respective Calculated $^{3}He/^{4}He$ Ratio Normalized to Ra

Sample	Li (ppm)	U (ppm)	Th (ppm)	Calculated R/Ra ratio
Lγ3CA	7.39	10.2	24	0.0019
γ4CA	10.8	6.93	26	0.0032
γ3CA	26.2	6.51	9.35	0.012
γMqL	26.2	2.77	11.1	0.019

Table 3
Concentrations and Fluxes of He-N_2-CH_4 in Caldanelle and Guagno-Les-Bains

Sites gas	Vol%	Gas flow ($L.h^{-1}$)	Free gas output ($mol.yr^{-1}$)	Water flow ($L.h^{-1}$)	R/Ra (free helium)	$^4He/^{20}Ne$ (free helium)	Dissolved gas concentration ($\mu mol.kg_w^{-1}$)	Dissolved gas output ($mol.yr^{-1}$)	R/Ra (dissolved helium)	$^4He/^{20}Ne$ (dissolved helium)	Total (m^3 $STP.yr^{-1}$)
Caldanelle		1.8		1,050							
He	1.45		9.23		0.06 Ra	110.6	52.5	483.7	n.m	n.m	11.1
N_2	98.28		627.02				4,154	38,238			874
CH_4	0.27		1.76				2.88	26.5			0.6
Guagno[a]		22		9,530							
He	1.21		91.54		0.02 Ra	36.1	51.5	4301.6	0.03 Ra	66.9	98.8
N_2	98.72		7437.60				4,113	343,615			7,893
CH_4	0.07		5.03				0.38	32			0.8

Note. n.m, not measured. STP stands for standard temperature and pressure (0°C, 1 bar). [a]Venturini spring + borehole combined springs with their respective R/Ra isotopic ratios.

primary spring to a depth of 200 m—remains relatively unaffected. Notably, the model delineates a conductive zone in close proximity to the Caldanelle hot spring, extending from the surface to an approximate depth of 150 m. Subjacent to this feature, the background resistivity exhibits a progressive increase with depth ranging from 2,000 to 5,000 Ω m (Figure 10). Figure S3 in Supporting Information S1 shows the misfit between the measured (point) and predicted (solid line) MT data at each site.

5. Discussion

5.1. Source of Water

Waters from both Caldanelle and Guagno exhibit similar sodium-chloride water types, indicative of high-temperature interactions between water and granitoid formations (Figure 6a; Bucher & Stober, 2010; Sonney, 2010; Stober & Bucher, 2007), while their chemical profiles are consistent with circulation through a granitic basement (Figure 6b).

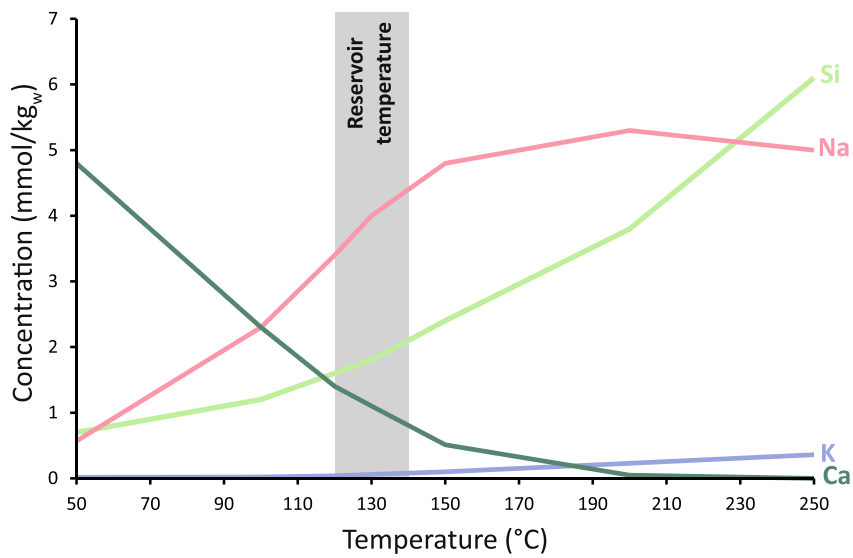

Figure 7. Concentrations of Si, Na, K, and Ca of a Na-Cl bearing water (5 $mmol/kg_w$ NaCl) equilibrated with primary and secondary minerals typical of granite hydrothermal alteration (see text) at temperatures ranging from 50 to 250°C. The modeled concentration of these elements matches the one measured at Caldanelle and Guagno for temperatures ranging from 120 to 140°C (gray area).

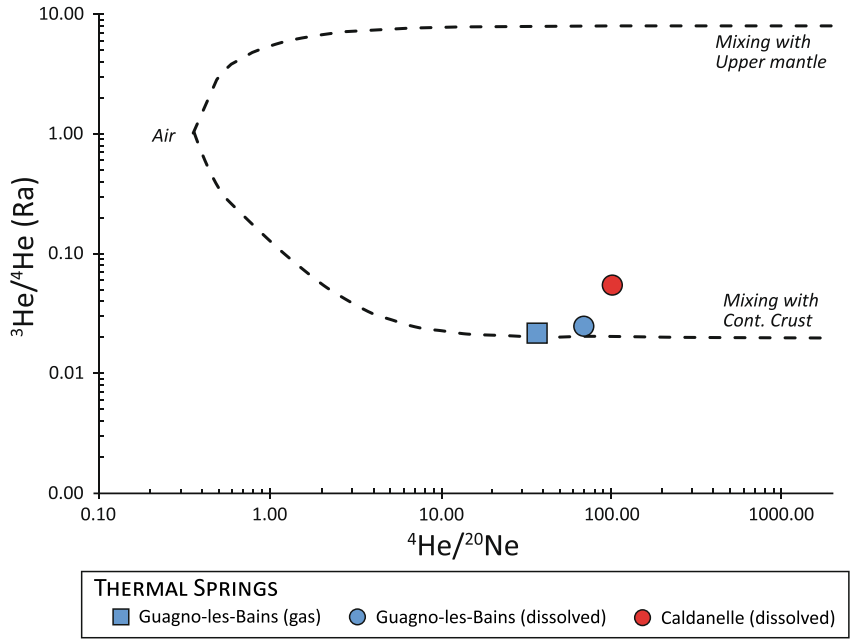

Figure 8. Relationship between the helium isotopic ratios (R/Ra values) and the $^4He/^{20}Ne$ ratios for dissolved and bubbling gases (only for Guagno).

Due to elevated $SiO_{2(aq)}$/temperature ratios in both springs, conventional silica geothermometers are unsuitable for application, likely due to secondary precipitation of amorphous silica during upwelling. As an alternative, sodium-potassium (Na/K) geothermometers were employed. However, these calculated temperatures serve only as approximations, necessitating corroboration with other geothermometric methods. The Na/K geothermometer proposed by Fournier (1979) was cross-referenced with results from corrected Na/K and Na/Li thermometers as per Michard (1979, 1990), Arnórsson et al. (1983a, 1983b), and Kharaka et al. (1982). All methods yielded consistent mean reservoir temperatures, ranging between 125 and 135°C for both Caldanelle and Guagno, corresponding to depths of 3–4 km, assuming a thermal gradient of 30 and 40°C/km. Reservoir temperatures were further corroborated through reverse modeling using the PhreeqC geochemical code (Parkhurst & Appelo, 2013) together with the LLNL thermodynamic database (Delany & Lundeen, 1991; Johnson et al., 2000). A simplified NaCl-bearing water (5 mmol/kg_w NaCl) was equilibrated at varying temperatures (ranging from 50 to 250°C, in 10°C increments) with a granitic mineralogy (quartz, K-Feldspar, anorthite, albite) allowing the precipitation of secondary minerals (kaolinite, saponite, montmorillonite). The resulting solution's temperature-dependent evolution, depicted in Figure 7, corroborates prior geothermometric estimations, suggesting water-granite interactions at temperatures between 120 and 140°C.

Isotopic analyses (δD-$\delta^{18}O$) conducted by Berthier et al. (1980) traced the origin of the waters to meteoric sources, with similar recharge altitudes ranging between 1,850 and 2,100 m. Radiocarbon dating estimated the circulation time of Guagno's water, which exhibits a higher surface temperature of 60°C, to be approximately 6,000 years (Berthier et al., 1980). In contrast, Caldanelle's water has a longer residence time of around 9,500 years (Berthier et al., 1980). These disparities in surface temperatures and residence times can be attributed to Guagno's faster water ascent and closer proximity to the reservoir and/or potential mixing with colder water in Caldanelle. Nevertheless, the similar chemical and isotopic compositions of the two sources tend to rule out the mixing hypothesis, suggesting a common reservoir within the batholith or the same stage of chemical evolution.

5.2. Origin of Helium

The concentration of helium in groundwater is influenced by multiple factors: atmospheric helium input, in situ radiogenic production from the reservoir's constitutive rocks, and external fluxes originating from the mantle and/or deep crust (Andrews, 1985; Heaton, 1984; Stute et al., 1992; Torgersen & Clarke, 1985). Helium isotopes serve as tracers for elucidating interactions among the atmosphere, crust, and mantle. Primordial ^3He is a vestige from

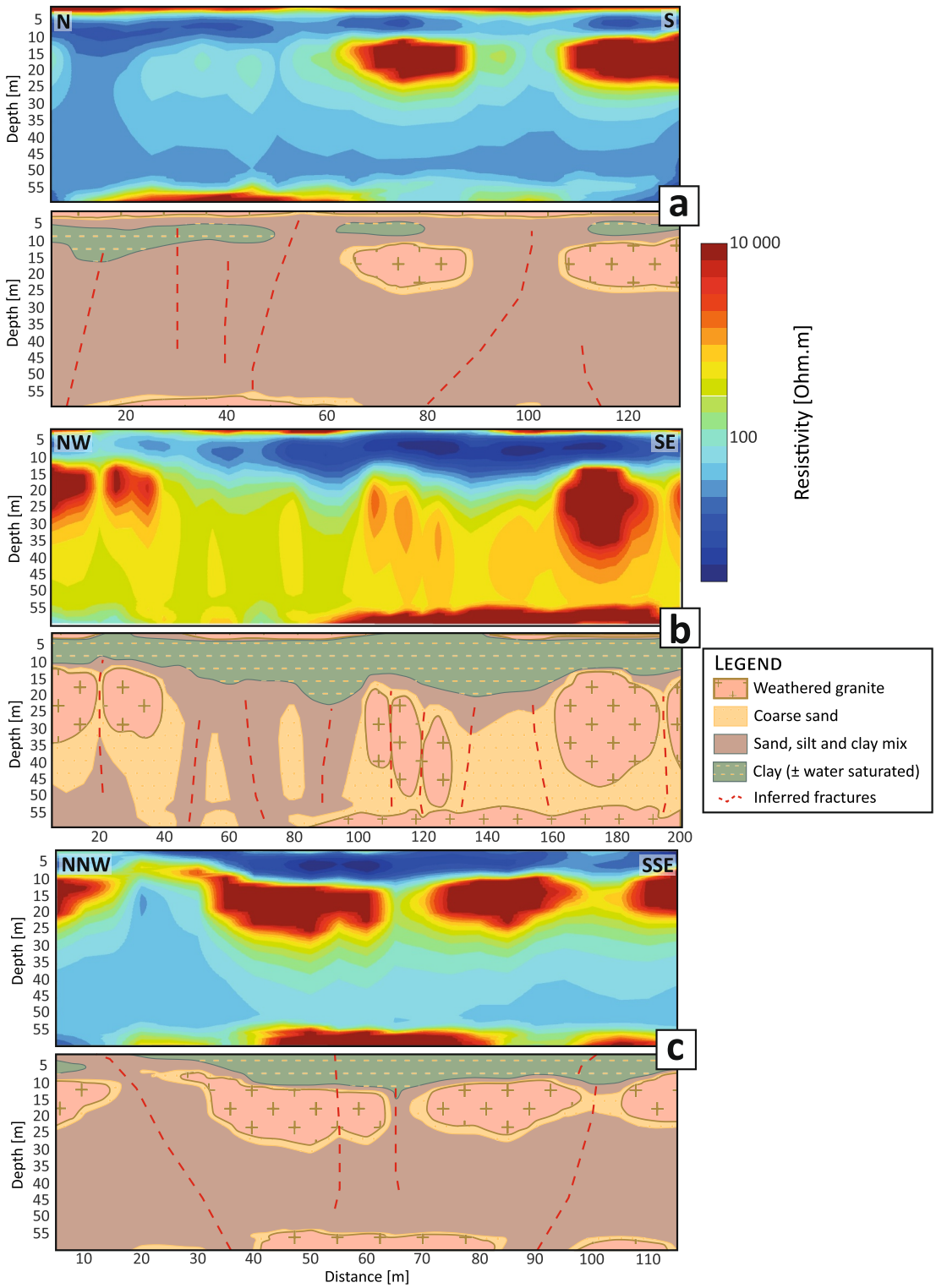

Figure 9. Electrical resistivity cross-sections from EMI data a, b, and c and their respective interpretations. See Figure 5b for location.

Earth's formation and serves as an indicator of deep sources such as the mantle. Additionally, ^{3}He can be generated to a lesser extent from ^{6}Li through neutron-alpha (n, α) reactions (Ballentine & Burnard, 2002). ^{4}He is predominantly generated by the radioactive decay of uranium (U) and thorium (Th) series radionuclides, making it ubiquitously present in the Earth's crust. Given that ^{20}Ne is largely derived from the atmosphere, the ^{3}He/^{4}He

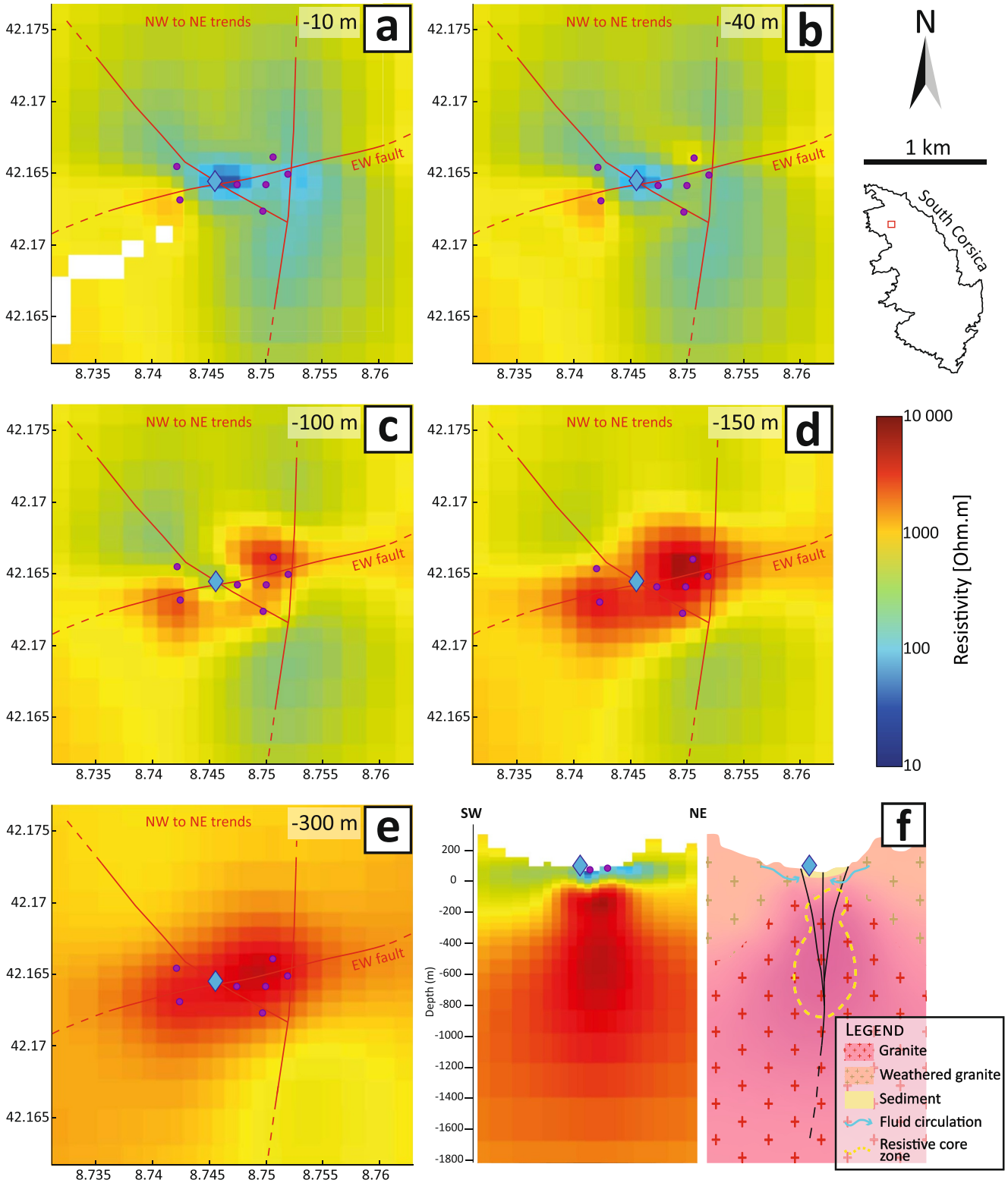

Figure 10. Panels (a–e) interpreted horizontal model resistivity sections from MT data. F, a resistivity cross section with its interpretation. The blue diamond corresponds to the Caldanelle main spring and the purple dots correspond to the MT measurement points. The length scale is the same horizontally and vertically.

ratio is frequently correlated with the $^4He/^{20}Ne$ ratio to assess potential atmospheric contamination during sampling and/or evaluate the amount of radiogenic helium that has been added to the initial recharge isotopic composition in equilibrium with the atmosphere. The typical end-member R/Ra ratio for continental crust is 0.02 Ra, where Ra represents the atmospheric ratio ($^3He/^4He = 1.4 \times 10^{-6}$). In contrast, the upper mantle (or more rigorously MORB) end-member is 8 ± 1 Ra (Ballentine & Burnard, 2002).

In Caldanelle and Guagno springs, the observed R/Ra ratios for helium in both aqueous and gaseous phases ranged from 0.02 to 0.06 Ra, indicating a predominantly crustal origin (Figure 8, Table 3). The $^4He/^{20}Ne$ ratio, between 36 and 111 (compared to the ASW $^4He/^{20}Ne$ ratio of 0.26), negates any significant atmospheric contribution to the overall helium production (Figure 8). Utilizing a typical upper crust composition and the measured U-Th-Li content from rocks proximal to the two studied springs, the calculated theoretical R/Ra ratios are between 0.0019 Ra and 0.019 Ra (Table 2; Andrews, 1985; Ballentine & Burnard, 2002). Compared to the measured R/Ra ratios, there is a partial agreement between the upper bound of the local production value (0.019 Ra) and that of the free phase measured in Guagno at 0.02 Ra. On the other hand, Guagno's dissolved helium shows higher R/Ra ratios. Such value could either be indicative of an atypical rock composition not present at the surface (an equivalent to γMqL but containing ≈80 ppm of Li, or Li-enriched pegmatites) or suggest a very slight mantle contribution. This means in theory that the measured R/Ra ratio exceeding 0.02 results from a small mantle contribution and that the helium production does not solely come from the granite-hosted reservoir. Assuming a crustal radiogenic end-member R/Ra ratio of 0.02 Ra and a mantle end-member of 8 Ra, it is estimated that up to 0.5% of He originates from the mantle.

Based on the in situ ^4He production rate, Torgersen (1980) proposed a simple analytical model to calculate the water residence time in sedimentary basins (see also Zhou & Ballentine, 2006). Here, this model is adapted and tested for a granitic environment. Under the assumption that radiogenic ^4He originates from U-Th decay within the granitic reservoir rocks, and given the known residence times of the waters from both springs, the in situ ^4He production rate within the aquifer can be quantified according to Equation 1.

$$[He]_{in\ situ} = \frac{\rho R_{4He} \Lambda (1-\varphi)}{\varphi} \times t \quad (1)$$

Here, $[He]_{in\ situ}$ represents the in situ ^4He production rate in m^3 STP $^4He/m^3$ of groundwater (STP stands for Standard Temperature and Pressure of 0°C and 1 bar, respectively), ρ denotes the aquifer density (assumed to be 2.75 g cm^{-3}, typical for granite), R_{4He} is the radiogenic ^4He production rate of the granitic basement, ϕ is the effective porosity (assumed to be 5%), t is the residence time in years (6,000 years in Guagno and 9,500 years in Caldanelle), and Λ is the ^4He transfer parameter from the rock matrix to the groundwater. The R_{4He} production rate is determined based on the highest U-Th content among the four analyzed lithologies, that is, [U] = 10.2 ppm and [Th] = 26 ppm, using Equation 2 from Craig and Lupton (1976):

$$R_{4He} = 0.2355 \times 10^{-12} \times [U] \times \left[1 + 0.123 \times \left(\frac{[Th]}{[U]} - 4\right)\right] \quad (2)$$

The transfer parameter (Λ) is commonly set to 1 as diffusion on geological timescales in sedimentary basins is fast (Torgersen & Clarke, 1985). However, this may not hold true for granitic basements. In any case, given the elevated temperatures of the reservoir, it is likely that most, if not all, in situ produced helium is released from the matrix to the groundwater. In Caldanelle and Guagno, the calculated in situ production rate is 1.5×10^{-6} m^3 STP $^4He/m^3$ of groundwater (or 6.77×10^{-5} mol/m^3), assuming a porosity of 5%. As no data on porosity are available, this value is chosen as representative of a granite porosity enhanced by the presence of faults and fractures. Calculations with lower (2%) and higher (10%) porosity have been performed to evaluate the sensitivity of our model to this parameter. A lower porosity of 2% returns an in situ He production rate 2.5 times higher and implies a 100% in situ sourced helium. Conversely, a porosity of 10% divides by two the calculated in situ production and hence calls for an important external input of helium. As the total ^4He surface flux in these springs is 3.51×10^{-6} m^3 STP $^4He/m^3$ of groundwater (or 1.56×10^{-4} mol/m^3), the in situ contribution can account for approximately 43% of the total ^4He production (Table 4). This highlights that the primary ^4He source might be external.

Table 4
Summary of Measured and Calculated Fluxes of ^{4}He for Caldanelle and Guagno Thermal Springs

Spring	Surface ^{4}He flux	Total surface ^{4}He flux	In situ ^{4}He flux	Total in situ ^{4}He flux	External ^{4}He flux	Total external ^{4}He flux
	μmol/m^3 of groundwater					
Caldanelle	53.1	156.3	41.5	67.7	89.7	146
Guagno	103.2		26.2		56.6	

Torgersen and Clarke (1985, 1987), Torgersen and Ivey (1985), Torgersen (1989), and Torgersen et al. (1992), along with Bethke et al. (1999), developed and employed a steady-state model to account for elevated He concentrations in the Great Artesian Basin of Australia. This model postulates that the entire source-crust volume releases its radiogenic ^{4}He into the groundwater system at the same rate as it is produced (Equation 3).

$$[\mathrm{He}]_{\text{external flux}} = \frac{\rho R_{4\mathrm{He}(dc)} H}{\varphi h} \times t \tag{3}$$

Where $R_{4\mathrm{He\ (dc)}}$ represents the radiogenic ^{4}He production rate of the deep crust, H is its thickness, and h is the thickness of the aquifer. The Corsican granitic batholith has an approximate thickness of 12 km and is underlined by a 6 km thick Eo-Variscan gneissic basement characterized by high radiogenic heat production and, consequently, an elevated ^{4}He production (Verdoya et al., 1998). At this depth, the closure temperature of most, if not all, the He-bearing minerals (mostly biotite, monazite and zircon) is exceeded so that the helium diffuses easily to the porosity. Assuming that the Eo-Variscan basement serves as the source for the external ^{4}He flux and that the granitic fractured reservoir is situated at a depth of 4 km, the maximum external ^{4}He flux for Caldanelle and Guagno is estimated to be 3.3×10^{-6} m^3 STP ^{4}He/m^3 of groundwater (or 1.46×10^{-4} mol/m^3), accounting for 93% of the measured surface flux (Table 4). Here, $R_{4\mathrm{He\ (dc)}}$ was calculated using Equation 2, assuming uranium and thorium contents of 4 and 19 ppm, respectively (Lucazeau & Mailhé, 1986; Verdoya et al., 1998), and a porosity of 2% for the gneiss basement (all the used parameters are displayed in Table S1 of Supporting Information S1).

These calculated He fluxes highlight that the contributions of the in situ production and the external flux are respectively of 31.6% and 68.4% to the total helium. Based on (a) the ^{4}He production rate of the batholith (i.e., 1.9×10^{-15} m^3/kg rock/year) and the Eo-Variscan gneissic basement (i.e., 1.02×10^{-15} m^3/kg rock/year), (b) their porosity and density, (c) the respective circulation time of Caldanelle and Guagno waters, and (d) assuming no helium loss, it is calculated that 0.3 and 6.0 km^3 of batholith granite and Eo-Variscan gneissic basement are required every year to generate the He production measured in Caldanelle and Guagno, respectively. This simple mass balance calculation highlights the fact that the drained volume of rock is rather low and implies that only the close vicinity of the faults acting as migration paths is drained.

The rate of ^{4}He production is generally insufficient to establish a continuous advective flow, and diffusion alone is inadequate for significant ^{4}He transport. Therefore, the migration of ^{4}He from the deep crust to the reservoir depends on the characteristics of the migration pathways (i.e., permeability and tortuosity), the behavior of the carrier fluid within these structures, and the frequency of tectonic events. Variscan Corsica is extensively fractured and structured by deeply rooted faults that offer efficient fluid migration pathways. ^{4}He can readily diffuse through these structures (Aldana Martinez, 2018; Barrocu, 2007). Moreover, given that seismic events on a 10,000-year timescale are common in Corsica (Larroque et al., 2021), the assumption of a steady-state crustal degassing model offers a valuable initial insight into the ^{4}He system of Caldanelle and Guagno.

5.3. Migration Pathways

The summed production rate of radiogenic ^{4}He accounting for both in situ and external fluxes is 4.8×10^{-6} m^3 STP ^{4}He/m^3 of groundwater (or 2.14×10^{-4} mol/m^3). Assuming that this value represents an upper production limit, approximately 27% of the generated ^{4}He is lost during its ascent to the surface. Given that the majority of helium is produced at depths exceeding 10 km, this loss is relatively modest. This suggests that deeply rooted pathways, such as faults and fractures in the Variscan batholiths, promote efficient He migration.

The intersection between the north-south (NS) fault and fracture fields—structures with orientations ranging from NNW-SSE to NNE-SSW—and the east-west (EW) structure in both Caldanelle and Guagno likely enhances permeability, thereby enabling fluid migration from the reservoir to the surface (Curewitz & Karson, 1997). Notably, N-S trending faults, which are the sole structures exhibiting thermal seeps, likely play an important role in fluid transport from meteoric sources to the reservoir. Other factors could also influence fault permeability, such as the nature of the rock, the intensity of deformation, the age of the structures and the type of movement recorded by the faults. However, externally sourced ^{4}He requires deep migration pathways to transfer to overlying reservoirs. The EW and NS to NNE-SSW fault orientations are pervasive in Variscan Corsica. According to Berthier et al. (1980), these orientations correspond to the dip of the massif beneath its basement, resulting in the observed NS to NNE-SSW fracture fields and relays. Additionally, the western segment of the major EW fault, upon which Caldanelle and Guagno are situated, features an exceptionally thick core zone of 20 m in Murzo. A core zone of hundreds of meters such as the one observed close to Guagno would imply a fault displacement of several kilometers, which is very unlikely. This core zone is probably the result of multiple faults coupled to a strong alteration of the damaged zone. In any case, a multi-kilometer-long fault with such a significant core thickness implies substantial displacement. Consequently, this EW structure is hypothesized to be deeply rooted, potentially extending beyond 10 km into the Earth's crust (Mayolle et al., 2019; Shipton et al., 2006; Torabi & Berg, 2011). Given the absence of substantial core zones in NS faults, the EW fault is assumed to serve as the primary conduit for deeply sourced He.

Ground resistivity surveys serve as effective tools for delineating physical characteristics such as water content, permeability, and lithologies, ranging from the meter scale (Electromagnetic Methods, EMI) to the kilometer scale (Magnetotelluric Methods, MT). These surveys are particularly useful for identifying faults, fractures, and fluid circulations. In a granitic bedrock, the presence of conductive fluids is expected to reduce the medium's resistivity, despite granite's inherently high resistive nature. The permeability of faulted and/or fractured zones as well as the rock's porosity plays a significant role. A crushed or fractured zone with elevated permeability is likely to exhibit either high resistivities if it is impermeable to fluids, or conversely, very low resistivities if it channels conductive fluids.

Surface observations reveal that the Caldanelle field is characterized by N45 to N90 elliptical structures of arenized granite (comprising sand and boulders) interspersed with sporadic zones of water-saturated clay. Based on these observations, the three previously defined units on the acquired EMI cross-sections can be interpreted (Figure 9). The upper resistive layer likely corresponds to arenized granite, while the lower conductive layer is attributable to water-saturated clay. Given that resistivity is sensitive to water content, the heterogeneous second unit is likely a composite of sand and clay derived from granitic material with variable water content. The rounded resistive anomalies are likely boulders of weathered, yet water-impermeable granite. While the third unit could potentially represent the upper boundary of a substantial granitic structure, the depth limitations of EMI acquisition complicate this interpretation. These units are locally truncated by sub-vertical structures with lower resistivities, particularly affecting the granite boulders in the second unit. These structures could be attributed to fractures or to artifacts related to the inversion, but the abundance of faults and fractures in the area points to the first hypothesis. However, none of them exhibit clear indications of fluid drainage.

Given that the fluids seeping in Caldanelle require migration pathways connecting the deep environment to the surface, the depth imaging provided by Magnetotelluric Methods (MT) is more appropriate, despite its lower resolution.

From the 3D MT model, five horizontal sections at depths of 10, 40, 100, 150, and 300 m are extracted. Based on prior interpretations from the EMI data and the background resistivity of the MT model, Figures 10a–10e demonstrate that weathering can reduce granite resistivity by an order of magnitude. This is corroborated in Figure 10f, where the resistivity of granite is approximately 5,000 Ω·m at depth and diminishes as it gets closer to the surface. Furthermore, the water in Caldanelle exhibits a conductivity range between 0.04 and 0.06 S m, corresponding to an average resistivity of 20 Ω m. Glover et al. (2000) developed a mixing model based on a modified Archie's law that returns the bulk resistivity of two conductive phases for any volume fraction and variable porosities and connectivities. Based on the granite and water conductivities, the bulk resistivity is expected to range from 500 to 2,000 Ω m for a well-connected porosity of 5% of the granite and to reach 10,000 Ω m for as the connectivity reduces, which is likely to occur as the depth increases (Figure 11). Using a lower porosity of 2% return bulk resistivities that are too high compared to what is imaged by the EMI and the MT results. A 10%

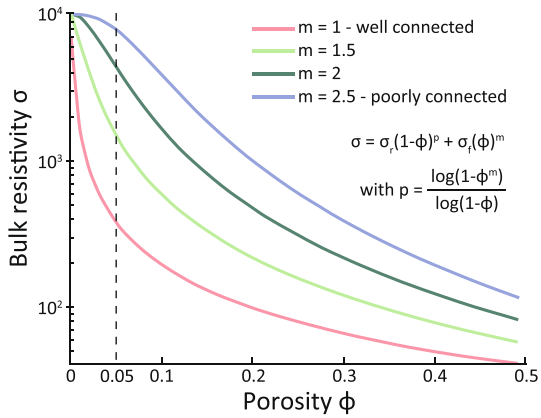

Figure 11. Bulk resistivity as a function of porosity (φ) and pore connectivity (m) after modified Archie's law (Glover et al. (2000)). Here, rock conductivity (σ_r) is 10^{-4} S/m (10 kΩ), fluid conductivity (σ_f) is 0.05 S/m (20 Ω). Broken blue line shows porosity of 5% assumed in section origin of helium.

porosity has the opposite effect. Consequently, the migration pathways for the waters under study should manifest as regions of lower resistivity. The notably low resistivities around Caldanelle's main spring underscore the thermal water circulations. This anomaly is readily identifiable near the surface as the mean resistivity of the granite is attenuated due to weathering. On its eastern side, it follows the river northward and extends southward. On its western side, the anomaly also follows a NW trend to the north of the main source, while on the southern side of the river and west of the main spring, it quickly reverts to background resistivity levels. The northward extension of this conductive area aligns well with the observed thermal fluid drainage patterns along the NW to NE-oriented faults and fracture systems (Figure 5b). Field observations confirm that fluid seepage occurs solely on the northern side of the main spring, which is consistent with the MT model. Assuming that this conductive anomaly is indicative of fluid ascent, it is plausible that part of the northern fault system extends southwards to the east of the spring, facilitating fluid drainage (Figure 10).

An east-west (EW) oriented resistive trend is obscured near the surface due to the presence of the conductive anomaly but becomes clearly discernible at greater depths (Figures 10d and 10f). This resistive feature extends to depths of approximately 1,600 m and is likely to correspond to the EW-oriented fault and fracture systems observed at the surface. Nevertheless, the geometry of this resistive unit is not well defined, probably as a result of the lack of north-south extension of survey points. However, the elevated resistivity within the core zone of this fault (Figures 10d–10f) suggests that this particular orientation is not serving as a conduit for thermal waters. This observation aligns with surface data, indicating that a thick, finely crushed core zone can indeed be impermeable to fluid flow, although surface permeability does not guarantee depth permeability and vice versa. Moreover, this core zone is particularly resistive between 100 and 1,000 m depth, suggesting that the interaction between the EW fault and the NW to NE-oriented faults and fractures system results in a highly impermeable unit (Figure 10f). However, this influence diminishes at depths greater than 1 km. This supports the previous assumption of a very deep EW fault and indicates that NW to NE faults and fractures are not deeply rooted in the batholith.

Given that the reservoir depth is estimated to be between 3 and 4 km and that NS faults and fractures are identified as the primary migration pathways for thermal water, one would expect to observe low resistivities extending from great depths to the surface. However, this is not the case. It is possible that the deep migration of thermal water occurs upstream of the Caldanelle area potentially through another unidentified fault system (i.e., not the EW faults and fractures systems). Consequently, the subsurface flow of water may be primarily influenced by topographical features, facilitated by NW- to NE-oriented faults and fractures.

5.4. Thermal Water Reservoir and Potential Helium Traps

As mentioned previously, thermal waters of Caldanelle and Guagno share the same chemical evolution and possibly a common reservoir within the granitic basement. These thermal fluids preferentially migrate through NW-SE to NE-SW subvertical structures, with seepages occurring exclusively to the north of the major EW fault. Hence, the dense fault and fracture networks are likely to constitute the reservoir with its configuration controlled by the permeability contrast between the different granitoids and the EW fault core zone acting as a barrier. This reservoir likely encompasses the northern part of the granitic unit intersected by the EW fault.

This reservoir also plays a role in the helium concentration process. Specifically, the previously determined ^{4}He contribution from the reservoir rocks was based on residence times of 9,500 and 6,000 years for Caldanelle and Guagno, respectively. These residence times may have an effect on helium concentration. On the other hand, a 27% discrepancy between the total He flux (sum of in situ production and external flux of ^{4}He) and the measured surface flux was calculated. In a steady state model, this could be attributed to a coupling effect of advective loss of helium through secondary faults and to a lesser extent diffusion loss. Indeed, the granitoids contain more radionuclides and therefore can produce more He than the underlying Eo-Variscan basement made of metamorphic rocks (see Section 5.2). However, the relatively high fracture density of the batholith, and hence increased porosity could facilitate the escape of He via secondary fault networks, which may explain why the

main production of ^{4}He is not in situ. In a scenario implying accumulation processes the migration of the ascending gas could be hindered by partial trapping allowing only a limited flux to escape toward the surface. The fault and fracture networks responsible for draining thermal fluids could exhibit varying physical characteristics such as lower permeabilities or greater tortuosities in their damaged zone and act as partial traps by restricting the flow close to the reservoir.

5.5. Helium Potential of Variscan Batholith

The study of the Caldanelle and Guagno helium systems highlights key factors for He concentration in a Variscan batholith. It also reveals the importance of specific pathfinders and a dedicated workflow for He exploration in such geological settings. The observations and measurements detailed above demonstrate that an efficient He external flux from the Eo-Variscan basement (tonalitic and granitic gneiss) coupled to the in situ He production from the batholith-hosted reservoir is capable of generating a He-rich gas mixture. This can be achieved mainly through the presence of dense faults and fracture networks that efficiently drain the fluids from the deep crust to the surface and possibly allow the accumulation of thermal fluids with limited He loss throughout the process. These source and migration parameters are probably those of the utmost importance for helium concentration in this kind of geological setting, but other secondary parameters influence the final concentration. As an example, the presence of other species such as N_2—a carrier gas commonly associated with He (Ballentine & Lollar, 2002)—, CH_4 or CO_2 act to exsolve the helium out of the groundwater, which would impact the volume of dissolve versus free gas and may dilute the final gas mixture by increasing the gas volume. However, the timing of the interaction of the other gases may play a bigger role in the final volume of helium than the volume of the gases themselves. On the other hand, they may increase the total gas flux, consequently affecting the He flux. In Caldanelle and Guagno N_2 is predominant and may act as a carrier gas but the absence of CO_2 and the limited presence of CH_4 could result in a relatively high He content. Furthermore, although efficient helium traps are not commonly reported in Variscan granitic environments, their presence could modify the concentration and flux of He by accumulating it over time instead of releasing it steadily. Some Variscan batholiths overlaid by a sedimentary cover could therefore host He accumulations. However, the likelihood of He accumulation in the fault network is higher in heavily fractured Variscan batholith providing favorable conditions for helium concentration.

At the European scale, post-orogenic granite and Eo-Variscan metamorphic rocks are widespread in the massifs inherited from the Variscan orogeny (Franke, 1989, Figure 2). In addition, the observed N-S and E-W faults and fracture directions in Corsica correspond to well-known orientations of deeply rooted Variscan structures (Arthaud & Matte, 1975). Thus, the geological context in which Caldanelle and Guagno are embedded can be identified throughout Europe, such as the Massif Central in France, the north-western part of the Iberian massif or the Bohemian batholith in Austria, suggesting that many other locations share the necessary characteristics for helium concentration and migration. Therefore, the He-rich thermal systems in Corsica provide insights into the helium-bearing potential of Variscan batholiths in a broader context.

The abundance of deep faults and fractures in Variscan batholiths offers significant opportunities for fluid migration, even at great depths. Indeed, many thermal springs are documented in European Variscan massifs, some of which contain high concentrations of helium (Aires-Barros et al., 1998; Barker et al., 2000; Carvalho, 1996; Risler, 1974; Risler & Batard, 1978; Vrba, 1996). Obviously, these different massifs, although similar in some respects, may differ locally for a number of geological reasons. The external flow of helium from the Eo-Variscan metamorphic rocks being one of the essential elements, its distance from the surface or its lithology could significantly affect the observed helium flux at the surface. In addition, the physical characteristics of local migration pathways may not be suitable for efficient gas drainage. Nevertheless, the lack of billion-year-old He source rocks coupled to stable intra-cratonic basins offering efficient trapping will not promote both a high flux of helium and a significant reservoir. On the other hand, a younger geological province (i.e., a shorter geological time scale) diminishes the risk of resource loss. Therefore, a balance must be found between a long-elapsed time of production, stable drainage and capture conditions as well as minimal loss. Taken together, the observations reported in this study contribute to the development of a methodology for exploring and understanding He systems in Variscan geological contexts (Figure 12 and Table 5).

Finally, considering Caldanelle and Guagno as examples, the annual production of He in these two thermal springs roughly exceeds 100 m^3 STP/yr, equivalent to 10 bottles of gas of 50 L at 200 bar (the so-called B50 standard). Given this, it is unlikely that He exploitation in Caldanelle or Guagno would be profitable unless

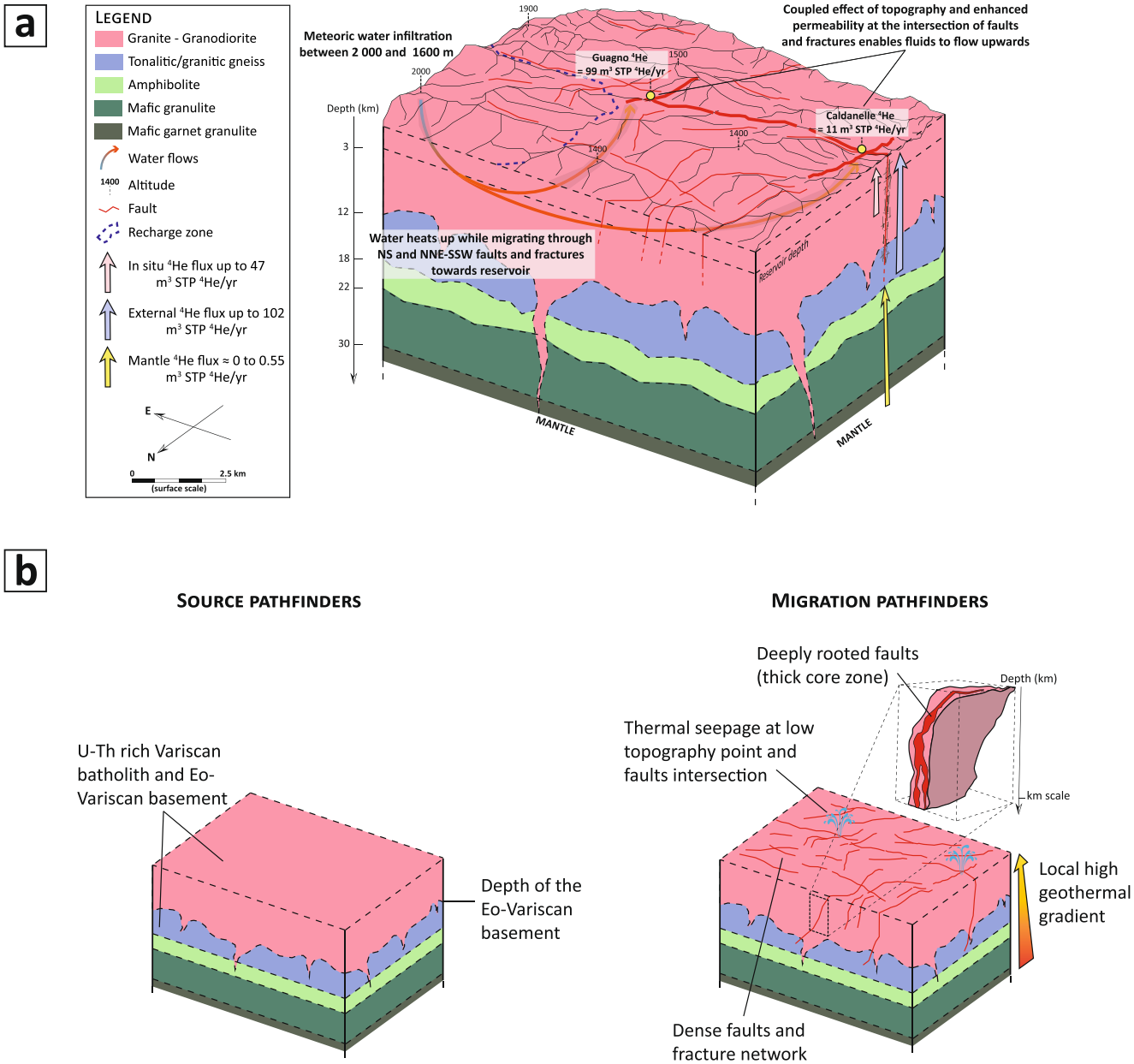

Figure 12. (a) schematic 3D block summarizing the thermal system of Caldanelle and Guagno-Les-Bains thermal springs and showing the source, migration and escape of helium. Layer geometry is not representative. (b) Schematic 3D block summarizing the source and migration pathfinders for helium exploration in a Variscan geological context.

identifying a deep reservoir and directly tapping into it. It is noteworthy that the 120 m deep borehole in Guagno already resulted in a He flow (both dissolved in water and as free gases) multiplied by about 10 compared to Caldanelle spring. Regardless, co-valorization of the geothermal resource will be mandatory.

6. Conclusions

This multi-disciplinary study of two Corsican thermal springs highlights the potential of Variscan batholiths in generating, concentrating, and mobilizing helium. Gas and rock chemistry coupled to analytical modeling show both the capacity of the Variscan rocks to generate He and the major contribution from the underlying Eo-Variscan basement. The presence of dense fracture networks and deeply rooted faults, as evidenced by the presence of secondary thermal seepage along N10 to N160 trending faults and corroborated by electro-magnetic

Geochemistry, Geophysics, Geosystems

10.1029/2024GC011519

Table 5
Methods, Criteria and Tools for He Exploration in a Variscan Geological Context

Target	Definition	Methodology and tools
Surface leakage indicators	He-bearing gas mixture bubbling in pool or springs, diffuse gas seeps in soils	- Existing literature data and field observations - Gas sampling and analysis (GC-TCD, MS) - Soil gas survey (portable gas sensors, radon detector to detect fluids circulations) - Infrared camera (to detect surface thermal anomaly) - Investigate local topography and hydrography (low topographic points)
Source	U-Th rich Variscan batholith and Eo-Variscan basement	- Geological map (target Variscan Late Carboniferous-Permian granites and Eo Variscan Devonian para and ortho gneisses) - Large scale geophysical survey (Bouguer and/or magnetic anomaly, seismic velocity, to investigate the structure of the crust) - Geochemistry of gases (stable isotopes and noble gases) and rocks (U-Th-Li concentrations) - Analytical Modeling
Migration path	Pluri-kilometric faults, permeable faults	- Geological map (target thick core zone, dense faults and fractures networks) - Field investigation (faults directions, draining faults) - Geophysical survey (electro-magnetic resistivities, magneto-telluric prospecting) - Geophysic and hydrologic modeling
Potential traps or seals	Mechanisms that delay or decrease the migration flow of He. Thick mudstones, salt, igneous intrusions or structural/stratigraphic traps	- Seismic and geological survey (well logs, stratigraphy, depth of inferred accumulation, fault networks/convergence of fluxes, fault properties)

and magnetotelluric surveys, appear to be key factors in controlling the migration of thermal fluids and the concentration of high He-bearing fluids (water and gas) within the Variscan geological context.

Remarkably, the measured helium concentrations, exceeding 1 vol%, surpass the averages found in various major helium production sites located within intra-cratonic sedimentary basins worldwide. This establishes Variscan batholiths as promising targets for He exploration. Through this comprehensive geological, geochemical, and geophysical approach, numerous indicators for the sourcing and migration of helium within Variscan batholiths have been identified. As such, this case study of Caldanelle and Guagno-Les-Bains provides guidance for helium exploration in similar Variscan contexts (Table 5).

However, the measured low helium fluxes suggest that economically viable extraction of this resource may not be feasible, at least on the basis of surface or low depth (less than 200 m) fluid analysis. The absence of billion-year-old helium source rocks poses challenges to both long-term production and accumulation. Nevertheless, the potential existence of an efficient trap could create an economically viable reservoir. Identifying the latter requires further investigations, opening avenues for future research and potential breakthroughs in helium resource exploration.

Data Availability Statement

Full data sets (Tables 1–4 and Table S1 in Supporting Information S1) supporting the interpretations and observations made in this study have been uploaded to a permanent online repository (Figshare, https://doi.org/10.6084/m9.figshare.25257388) where they will be made available to the public upon publication. The paleomap data set used for Figure 2c can be found online (https://www.earthbyte.org/paleomap-paleoatlas-for-gplates/) as well as GPlates software for visualization (Müller et al., 2018; https://www.gplates.org/). Phreeqc software for geochemical calculations as well as the LLNL used database are available respectively from https://www.usgs.gov/software/phreeqc-version-3 and https://seaborg.llnl.gov/resources/geochemical-databases-modeling-codes. EMagPy software for modeling and inversion of electromagnetic induction data is available from gitlab (https://gitlab.com/hkex/emagpy). All information about ModEM for inversion of electro-magnetic geophysical data can be found from (http://www.modem-geophysics.com/). The BDAlti topographical data set is available online from the Institut National de l'Information géographique et forestière, IGN (https://geoservices.ign.fr).

Acknowledgments
Authors acknowledge Andrea Perrin and Antonia Perrin (EARL Caldanelle) for access to their land and spa, Christophe Battesti for providing key information about the history of Guagno-Les-Bains thermal baths, as well as Aldric Donzé and Dimitri Laurent for their help with fieldwork. This article is part of a PhD funded by a ministerial grant (MESRI). This project has received funding from the French National Research Agency (Grant agreement ANR-20-CE01-0020). LT acknowledges support from the Institut Universitaire de France. Finally, the authors thank the reviewers for their invaluable feedback on the manuscript.

References

Aires-Barros, L., Marques, J., Graça, R. C., Matias, M. J., Van Der Weijden, C. H., Kreulen, R., & Eggenkamp, H. G. M. (1998). Hot and cold CO_2-rich mineral waters in Chaves geothermal area (northern Portugal). *Geothermics*, *27*(1), 89–107. https://doi.org/10.1016/S0375-6505(97)84483-5

Aldana Martinez, S. C. (2018). Assessment methodology of permeability in a granitic aquifer in a pilot basin in the south of Sardinia (Italy). Retrieved from https://hdl.handle.net/11584/255990

Andrews, J. N. (1985). The isotopic composition of radiogenic helium and its use to study groundwater movement in confined aquifers. *Chemical Geology*, *49*(1–3), 339–351. https://doi.org/10.1016/0009-2541(85)90166-4

Arnórsson, S., Gunnlaugsson, E., & Svavarsson, H. (1983a). The geochemistry of geothermal waters in Iceland. II. Mineral equilibria and independent variables controlling water compositions. *Geochimica et Cosmochimica Acta*, *47*(3), 547–566. https://doi.org/10.1016/0016-7037(83)90277-6

Arnórsson, S., Gunnlaugsson, E., & Svavarsson, H. (1983b). The geochemistry of geothermal waters in Iceland. III. Chemical geothermometry in geothermal investigations. *Geochimica et Cosmochimica Acta*, *47*(3), 567–577. https://doi.org/10.1016/0016-7037(83)90278-8

Arthaud, F., & Matte, P. (1975). Les décrochements tardi-hercyniens du sud-ouest de l'Europe. Géométrie et essai de reconstitution des conditions de la déformation. *Tectonophysics*, *25*(1–2), 139–171. https://doi.org/10.1016/0040-1951(75)90014-1

Ballentine, C. J., & Burnard, P. G. (2002). Production, release and transport of noble gases in the continental crust. *Reviews in Mineralogy and Geochemistry*, *47*(1), 481–538. https://doi.org/10.2138/RMG.2002.47.12

Ballentine, C. J., & Lollar, B. S. (2002). Regional groundwater focusing of nitrogen and noble gases into the Hugoton-Panhandle giant gas field, USA. *Geochimica et Cosmochimica Acta*, *66*(14), 2483–2497. https://doi.org/10.1016/S0016-7037(02)00850-5

Barker, J. A., Downing, R. A., Gray, D. A., Findlay, J., Kellaway, G. A., Parker, R. H., & Rollin, K. E. (2000). Hydrogeothermal studies in the United Kingdom. *The Quarterly Journal of Engineering Geology and Hydrogeology*, *33*(1), 41–58. https://doi.org/10.1144/qjegh.33.1.41

Barrocu, G. (2007). Hydrogeology of granite rocks in Sardinia. In *Groundwater in fractured rocks* (pp. 49–60). CRC Press.

Batard, F., Baubron, J. C., Bosch, B., Marcé, A., & Risler, J. J. (1982). Isotopic identification of gases of a deep origin in French thermomineral waters. *Journal of Hydrology*, *56*(1–2), 1–21. https://doi.org/10.1016/0022-1694(82)90053-1

Berthier, F., Demange, J., & Desplan, A. (1980). *Etude préliminaire des ressources géothermiques de la Corse* (Vol. 56). BRGM.

Bethke, C. M., Zhao, X., & Torgersen, T. (1999). Groundwater flow and the ^{4}He distribution in the Great Artesian Basin of Australia. *Journal of Geophysical Research*, *104*(B6), 12999–13011. https://doi.org/10.1029/1999JB900085

Brodie, R., & Jiang, W. (2018). Trans-dimensional Monte Carlo inversion of short period magnetotelluric data for cover thickness estimation. https://doi.org/10.1071/ASEG2018abT5_1F

Brown, A. (2019). Origin of helium and nitrogen in the Panhandle–Hugoton field of Texas, Oklahoma, and Kansas, United States. *AAPG Bulletin*, *103*(2), 369–403. https://doi.org/10.1306/07111817343

Bucher, K., & Stober, I. (2010). Fluids in the upper continental crust. *Geofluids*, *10*(1-2), 241–253. https://doi.org/10.1002/9781444394900.ch17
Cagniard, L. (1953). Basic theory of the magnetotelluric method of geophysical prospecting. *Geophysics*, *18*(3), 605–635. https://doi.org/10.1111/j.1468-8123.2010.00279.x
Cai, Z., Clarke, R. H., Glowacki, B. A., Nuttall, W. J., & Ward, N. (2010). Ongoing ascent to the helium production plateau—Insights from system dynamics. *Resources Policy*, *35*(2), 77–89. https://doi.org/10.1016/j.resourpol.2009.10.002
Caritg, S., Lahondère, D., & Rossi, P. (2009). *Carte Géologique Harmonisée du Département de la Corse du sud: Notice Explicative* (p. 298). BRGM.
Carvalho, J. M. (1996). Mineral water exploration and exploitation at the Portuguese Hercynian Massif. *Environmental Geology*, *27*(3), 252–258. https://doi.org/10.1007/BF00770439
Casini, L., Cuccuru, S., Puccini, A., Oggiano, G., & Rossi, P. (2015). Evolution of the Corsica–Sardinia Batholith and late-orogenic shearing of the Variscides. *Tectonophysics*, *646*, 65–78. https://doi.org/10.1016/j.tecto.2015.01.017
Chave, A. D. & Jones, A. G. (Eds.). (2012). *The magnetotelluric method: Theory and practice*. Cambridge University Press.
Cheng, A., Sherwood Lollar, B., Gluyas, J. G., & Ballentine, C. J. (2023). Primary N_2–He gas field formation in intracratonic sedimentary basins. *Nature*, *615*(7950), 94–99. https://doi.org/10.1038/s41586-022-05659-0
Cline, J. D. (1969). Spectrophotometric determination of hydrogen sulfide in natural waters. *Limnology & Oceanography*, *14*(3), 454–458. https://doi.org/10.4319/lo.1969.14.3.0454
Cortesogno, L., Cassinis, G., Dallagiovanna, G., Gaggero, L., Oggiano, G., Ronchi, A., et al. (1998). The Variscan post-collisional volcanism in late Carboniferous–Permian sequences of Ligurian Alps, southern Alps and Sardinia (Italy): A synthesis. *Lithos*, *45*(1–4), 305–328. https://doi.org/10.1016/S0024-4937(98)00037-1
Craig, H., & Lupton, J. E. (1976). Primordial neon, helium, and hydrogen in oceanic basalts. *Earth and Planetary Science Letters*, *31*(3), 369–385. https://doi.org/10.1016/0012-821X(76)90118-7
Curewitz, D., & Karson, J. A. (1997). Structural settings of hydrothermal outflow: Fracture permeability maintained by fault propagation and interaction. *Journal of Volcanology and Geothermal Research*, *79*(3–4), 149–168. https://doi.org/10.1016/S0377-0273(97)00027-9
Danabalan, D., Gluyas, J. G., Macpherson, C. G., Abraham-James, T. H., Bluett, J. J., Barry, P. H., & Ballentine, C. J. (2022). The principles of helium exploration. *Petroleum Geoscience*, *28*(2), petgeo2021-029. https://doi.org/10.1144/petgeo2021-029
Delany, J. M., & Lundeen, S. R. (1991). *The LLNL thermochemical data base: Revised data and file format for the EQ3/6 package* (No. UCID-21658). Lawrence Livermore National Laboratory (LLNL).
Derron, M. H., & Pfeifer, H. R. (2018). Caractérisation Hydrogéochimique Des Eaux de Source Alpines Hydrogeochemical Characterization of Alpine Spring Waters. *Bulletin de la Société Vaudoise des Sciences Naturelles*, *96*, 5–29.
Dong, M., Wang, Z. X., Dong, H., Ma, L. C., & Zhang, L. Y. (2019). Characteristics of helium accumulation in the Guanzhong Basin, China. *China Geology*, *2*(2), 218–226. https://doi.org/10.31035/cg2018103
Doolittle, J. A., & Brevik, E. C. (2014). The use of electromagnetic induction techniques in soils studies. *Geoderma*, *223*, 33–45. https://doi.org/10.1016/j.geoderma.2014.01.027
Fournier, R. O. (1979). A revised equation for the Na/K geothermometer. *Geothermal Resources Council - Transactions*, *3*, 221–224.
Franke, W. (1989). Tectonostratigraphic units in the Variscan belt of central Europe. *Geological Society of America Special Paper*, *230*, 67–90. https://doi.org/10.1130/SPE230-p67
GF Instruments. (2016). Short guide for electromagnetic conductivity mapping and tomography.
GF Instruments. (2020). CMD electromagnetic conductivity meters: User manual V2.3.
Giggenbach, W. F. (1988). Geothermal solute equilibria. Derivation of Na-K-Mg-Ca geoindicators. *Geochimica et Cosmochimica Acta*, *52*(12), 2749–2765. https://doi.org/10.1016/0016-7037(88)90143-3
Glover, P. W., Hole, M. J., & Pous, J. (2000). A modified Archie's law for two conducting phases. *Earth and Planetary Science Letters*, *180*(3–4), 369–383. https://doi.org/10.1016/S0012-821X(00)00168-0
Hao, Y., Kuang, X., Feng, Y., Wang, Y., Zhou, H., & Zheng, C. (2023). Discovery and genesis of helium-rich geothermal fluids along the India–Asia continental convergent margin. *Geochimica et Cosmochimica Acta*, *360*, 175–191. https://doi.org/10.1016/j.gca.2023.09.011
Heaton, T. H. E. (1984). Rates and sources of ^{4}He accumulation in groundwater. *Hydrological Sciences Journal*, *29*(1), 29–47. https://doi.org/10.1080/02626668409490920
Johnson, J., Anderson, G., & Parkhurst, D. (2000). Database from 'thermo.com.V8.R6.230' [Dataset]. *Prepared by at Lawrence Livermore National Laboratory*. (Revision: 1.11). Retrieved from https://seaborg.llnl.gov/resources/geochemical-databases-modeling-codes
Kelbert, A., Meqbel, N., Egbert, G. D., & Tandon, K. (2014). Modem: A modular system for inversion of electro-magnetic geophysical data. *Computers and Geosciences*, *66*, 40–53. https://doi.org/10.1016/j.cageo.2014.01.010
Kharaka, Y. K., Lico, M. S., & Law-Leroy, M. (1982). Chemical geothermometers applied to formation waters, Gulf of Mexico and California basins. *AAPG Bulletin*, *66*(5), 588. https://doi.org/10.1306/03b59eae-16d1-11d7-8645000102c1865d
Larroque, C., Baize, S., Albaric, J., Jomard, H., Trévisan, J., Godano, M., et al. (2021). Seismotectonics of southeast France: From the Jura mountains to Corsica. *Comptes Rendus Geoscience*, *353*(S1), 105–151. https://doi.org/10.5802/crgeos.69
Lucazeau, F. (1981). *Flux de chaleur, production de chaleur et évolution géodynamique récente du Massif Central Français* (Doctoral dissertation). Université des Sciences et Techniques du Languedoc; Montpellier II.
Lucazeau, F., & Mailhé, D. (1986). Heat flow, heat production and fission track data from the Hercynian basement around the Provençal Basin (western Mediterranean). *Tectonophysics*, *128*(3–4), 335–356. https://doi.org/10.1016/0040-1951(86)90300-8
Mabry, J., Lan, T., Burnard, P., & Marty, B. (2013). High-precision helium isotope measurements in air. *Journal of Analytical Atomic Spectrometry*, *28*(12), 1903–1910. https://doi.org/10.1039/C3JA50155H
Mayolle, S., Soliva, R., Caniven, Y., Wibberley, C., Ballas, G., Milesi, G., & Dominguez, S. (2019). Scaling of fault damage zones in carbonate rocks. *Journal of Structural Geology*, *124*, 35–50. https://doi.org/10.1016/j.jsg.2019.03.007
McLachlan, P., Blanchy, G., & Binley, A. (2021). EMagPy: Open-source standalone software for processing, forward modeling and inversion of electromagnetic induction data. *Computers & Geosciences*, *146*, 104561. https://doi.org/10.1016/j.cageo.2020.104561
Michard, G. (1979). Géothermomètres chimiques. *Bulletin du BRGM (2e série), Section, III*, *2*, 183–189.
Michard, G. (1990). Behaviour of major elements and some trace elements (Li, Rb, Cs, Sr, Fe, Mn, W, F) in deep hot waters from granitic areas. *Chemical Geology*, *89*(1–2), 117–134. https://doi.org/10.1016/0009-2541(90)90062-C
Müller, R. D., Cannon, J., Qin, X., Watson, R. J., Gurnis, M., Williams, S., et al. (2018). GPlates: Building a virtual Earth through deep time [Software]. *Geochemistry, Geophysics, Geosystems*, *19*(7), 2243–2261. https://doi.org/10.1029/2018GC007584
Nabighian, M. N. (Ed.) (1988). *Electromagnetic methods in applied geophysics: Volume 1, theory*. Society of Exploration Geophysicists. https://doi.org/10.1190/1.9781560802631

Olafsdottir, A. H., & Sverdrup, H. U. (2020). Assessing the past and future sustainability of global helium resources, extraction, supply and use, using the integrated assessment model WORLD7. *Biophysical Economics and Sustainability*, *5*(2), 6. https://doi.org/10.1007/s41247-020-00072-5

Parkhurst, D. L., & Appelo, C. A. J. (2013). Description of input and examples for PHREEQC version 3—A computer program for speciation, batch-reaction, one-dimensional transport, and inverse geochemical calculations. [Software]. *U.S. Geological Survey Techniques and Methods*, 497. book 6, chap. A43. https://doi.org/10.3133/tm6A43

Provornaya, I. V., Filimonova, I. V., Eder, L. V., Nemov, V. Y., & Zemnukhova, E. A. (2022). Prospects for the global helium industry development. *Energy Reports*, *8*, 110–115. https://doi.org/10.1016/j.egyr.2022.01.087

Risler, J. J. (1974). Description et classification géologique des sources minérales et thermales du Massif Central. *BRGM Report* (Vol. *74*).

Risler, J. J., & Batard, F. (1978). Helium et sources thermominerales en France. BRGM/78-SGN-684-MCE, 11 p. 3 pht.

Rossi, P., & Cocherie, A. (1991). Genesis of a Variscan batholith: Field, petrological and mineralogical evidence from the Corsica-Sardinia batholith. *Tectonophysics*, *195*(2–4), 319–346. https://doi.org/10.1016/0040-1951(91)90219-I

Rossi, P., Cocherie, A., & Fanning, C. M. (2015). Evidence in Variscan Corsica of a brief and voluminous Late Carboniferous to Early Permian volcanic-plutonic event contemporaneous with a high-temperature/low-pressure metamorphic peak in the lower crust. *Bulletin de la Societe Geologique de France*, *186*(2–3), 171–192. https://doi.org/10.2113/gssgfbull.186.2-3.171

Rossi, P., Marre, J., Cocherie, A., & Caballero, Y. (2010). *Notice explicative, Carte geol. France (1/50 000), feuille Vico-Cargese (1113)* (p. 156). BRGM. Carte geologique par Rossi Ph., Marre J. (2010.

Scotese, C. R., & van der Pluijm, B. A. (2020). Deconstructing tectonics: Ten animated explorations [Dataset]. *Earth and Space Science*, *7*(11), e2019EA000989. https://doi.org/10.1029/2019EA000989

Shipton, Z. K., Soden, A. M., Kirkpatrick, J. D., Bright, A. M., & Lunn, R. J. (2006). How thick is a fault? Fault displacement-thickness scaling revisited. https://doi.org/10.1029/170GM19

Sonney, R. (2010). *Groundwater flow, heat and mass transport in geothermal systems of a Central Alpine Massif. The cases of Lavey-les-Bains, Saint-Gervais-les-Bains and Val d'Illiez*. (Doctoral dissertation). Université de Neuchâtel.

Stober, I., & Bucher, K. (2007). Hydraulic properties of the crystalline basement. *Hydrogeology Journal*, *15*(2), 213–224. https://doi.org/10.1007/s10040-006-0094-4

Stute, M., Sonntag, C., Déak, J., & Schlosser, P. (1992). Helium in deep circulating groundwater in the Great Hungarian Plain: Flow dynamics and crustal and mantle helium fluxes. *Geochimica et Cosmochimica Acta*, *56*(5), 2051–2067. https://doi.org/10.1016/0016-7037(92)90329-H

Sumner, J. S. (2012). *Principles of induced polarization for geophysical exploration*. Elsevier.

Tikhnov, A. N. (1950). The determination of the electrical properties of deep layers of the earth's crust. *Doklady Akademii Nauk SSSR*, *73*, 295–297.

Torabi, A., & Berg, S. S. (2011). Scaling of fault attributes: A review. *Marine and Petroleum Geology*, *28*(8), 1444–1460. https://doi.org/10.1016/j.marpetgeo.2011.04.003

Torgersen, T. (1980). Controls on pore-fluid concentration of ^{4}He and ^{222}Rn and the calculation of $^{4}He/^{222}Rn$ ages. *Journal of Geochemical Exploration*, *13*(1), 57–75. https://doi.org/10.1016/0375-6742(80)90021-7

Torgersen, T. (1989). Terrestrial helium degassing fluxes and the atmospheric helium budget: Implications with respect to the degassing processes of continental crust. *Chemical Geology: Isotope Geoscience section*, *79*(1), 1–14. https://doi.org/10.1016/0168-9622(89)90002-X

Torgersen, T., & Clarke, W. B. (1985). Helium accumulation in groundwater, I: An evaluation of sources and the continental flux of crustal 4He in the Great Artesian Basin, Australia. *Geochimica et Cosmochimica Acta*, *49*(5), 1211–1218. https://doi.org/10.1016/0016-7037(85)90011-0

Torgersen, T., & Clarke, W. B. (1987). Helium accumulation in groundwater, III. Limits on helium transfer across the mantle-crust boundary beneath Australia and the magnitude of mantle degassing. *Earth and Planetary Science Letters*, *84*(2–3), 345–355. https://doi.org/10.1016/0012-821X(87)90098-7

Torgersen, T., Habermehl, M. A., & Clarke, W. B. (1992). Crustal helium fluxes and heat flow in the Great Artesian Basin, Australia. *Chemical Geology*, *102*(1–4), 139–152. https://doi.org/10.1016/0009-2541(92)90152-U

Torgersen, T., & Ivey, G. N. (1985). Helium accumulation in groundwater. II: A model for the accumulation of the crustal ^{4}He degassing flux. *Geochimica et Cosmochimica Acta*, *49*(11), 2445–2452. https://doi.org/10.1016/0016-7037(85)90244-3

Verdoya, M., Pasquale, V., Chiozzi, P., & Kukkonen, I. T. (1998). Radiogenic heat production in the Variscan crust: New determinations and distribution models in Corsica (northwestern Mediterranean). *Tectonophysics*, *291*(1–4), 63–75. https://doi.org/10.1016/S0040-1951(98)00031-6

Vrba, J. (1996). Thermal mineral water springs in Karlovy Vary. *Environmental Geology*, *27*(2), 120–125. https://doi.org/10.1007/BF01061684

Yurkowski, M. M. (2016). *Helium in southwestern Saskatchewan: Accumulation and geological setting*. *Open File Report* (Vol. 1, p. 20). Saskatchewan Ministry of the Economy, Saskatchewan Geological Survey.

Zhou, Z., & Ballentine, C. J. (2006). ^{4}He dating of groundwater associated with hydrocarbon reservoirs. *Chemical Geology*, *226*(3–4), 309–327. https://doi.org/10.1016/j.chemgeo.2005.09.030